

GalSyn I: A Forward-Modeling Framework for Synthetic Galaxy Observations from Hydrodynamical Simulations and First Data Release from IllustrisTNG

ABDURRO'UF ¹, HENRY C. FERGUSON ², SAMIR SALIM ¹, KARTHEIK IYER ³, LARRY D. BRADLEY ²,
DAN COE ^{2,4,5}, NOVAN SAPUTRA HARYANA ⁶, SULTAN HASSAN ², INTAE JUNG ⁷, GOURAV KHULLAR ^{8,9},
TAKAHIRO MORISHITA ⁶ AND LAMIYA MOWLA ¹⁰

¹*Department of Astronomy, Indiana University, 727 East Third Street, Bloomington, IN 47405, USA*

²*Space Telescope Science Institute (STScI), 3700 San Martin Drive, Baltimore, MD 21218, USA*

³*Flatiron Institute, 162 5th Avenue, New York, NY 10010, USA*

⁴*Association of Universities for Research in Astronomy (AURA), Inc. for the European Space Agency (ESA)*

⁵*Department of Physics and Astronomy, The Johns Hopkins University, 3400 N Charles St. Baltimore, MD 21218, USA*

⁶*Astronomical Institute, Tohoku University, 6-3, Aramaki, Aoba-ku, Sendai, Miyagi, 980-8578, Japan*

⁷*Department of Astronomy and Space Science, Chungbuk National University, Cheongju, 28644, Republic of Korea*

⁸*Department of Astronomy, University of Washington, Physics-Astronomy Building, Box 351580, Seattle, WA 98195-1700, USA*

⁹*eScience Institute, University of Washington, Physics-Astronomy Building, Box 351580, Seattle, WA 98195-1700, USA*

¹⁰*Department of Physics and Astronomy, Wellesley College, Wellesley, MA 02481, USA*

ABSTRACT

We present GalSyn (Galaxy Synthesizer), a modular and flexible Python package for generating synthetic spectrophotometric observations from hydrodynamical galaxy simulations. GalSyn employs a particle-by-particle spectral modeling approach that enables the rapid production of large synthetic datasets required for statistical population studies, offering a computationally efficient alternative to full radiative transfer codes. Users have full control over the spectral modeling choices, including the choice of stellar population synthesis engine, stellar isochrones, spectral libraries, and initial mass functions. Dust attenuation is modeled at the spatially resolved level via a line-of-sight column density method, with a comprehensive suite of fixed and adaptive attenuation laws. A decoupled kinematics model independently Doppler-shifts the stellar and nebular components, enabling realistic synthetic IFU data cubes. It also provides features to add observational realism, including PSF convolution and multi-component noise simulation. Beyond imaging and spectroscopic data cubes, GalSyn reconstructs spatially resolved physical property maps and star formation histories. Alongside this paper, we present the first public data release of synthetic imaging observations and spatially resolved star formation histories generated from the IllustrisTNG simulation suites, comprising four mock extragalactic survey fields (with areas of 5, 8, 137, 365 arcmin²), progenitor histories of 290 local massive galaxies ($\log(M_{*,z=0}/M_{\odot}) > 10.5$) tracked across $0 < z < 5$, and 259 major-merger systems. Each galaxy data cube contains imaging in 47 filters spanning HST, JWST, Euclid, Rubin/LSST, and the Roman Space Telescope. GalSyn is publicly available at <https://github.com/aabdurruf/GalSyn>.

Keywords: Galaxies (573) — High-redshift galaxies (734) — Hydrodynamical simulations (767) — Galaxy formation (595) — Galaxy evolution (594)

1. INTRODUCTION

The current era of astronomical research has seen an unprecedented influx of observational data. The advent of state-of-the-art telescopes and surveys, including the *James Webb Space Telescope (JWST)* (J. P. Gardner et al. 2023; J. Rigby et al. 2023), the *Euclid* mission (Euclid Collaboration et al. 2025), the *Vera C. Rubin Observatory* (Ž. Ivezić et al. 2019), and the upcoming

Nancy Grace Roman Space Telescope, has opened a new paradigm of “big data” in astronomy. These powerful instruments are capable of observing galaxies with unprecedented depth, spatial resolution, and field of view, generating datasets that are orders of magnitude larger and more complex than those previously available. However, this wealth of observational data presents both opportunities and challenges. While it enables detailed

studies of galaxy properties and their evolution, it also demands sophisticated theoretical frameworks and computational tools capable of bridging the gap between numerical simulations and observational results.

Forward modeling and synthetic observations have emerged as an important component in this endeavor, serving as essential intermediaries between theoretical models and real observations. By creating mock observations from simulations, we can directly compare theoretical predictions with observational data, validate galaxy formation models, and interpret complex observational signatures. This approach is particularly crucial in the field of galaxy evolution, where the interplay between various physical processes (e.g., star formation, feedback processes, and chemical enrichment) produces complex observational signatures that could be better understood through detailed forward modeling.

A crucial component in the forward modeling is computing the emergent spectrum from a collection of stars, gas, and dust in the interstellar medium (ISM) of a galaxy, which is very complex. Radiative transfer (RT) techniques, exemplified by codes such as SKIRT (P. Camps & M. Baes 2015, 2020), SUNRISE (P. Jonsson 2006), and POWDERDAY (T. P. Robitaille 2011; D. Narayanan et al. 2021), can be applied to track the propagation of photons through the ISM, accounting for absorption, scattering, and re-emission. However, these codes do not themselves model the emergent spectrum of a given stellar population. Furthermore, the emergent spectrum of the “star particles” in a simulation ought to, in principle, include both a composite population of stars and the effects of the local sub-grid ISM on this emergent spectrum.

The primary advantage of RT codes lies in their physical accuracy and self-consistency. They naturally capture phenomena such as dust heating, cooling, and scattered light contributions. However, this accuracy comes at a substantial computational cost. Radiative transfer calculations are computationally intensive, often requiring significant computational resources and time, particularly for high-resolution simulations or large galaxy samples. This computational burden can limit the exploration of parameter space and the generation of large synthetic datasets required for statistical studies.

An alternative approach has emerged in the form of particle-by-particle spectral modeling, as implemented in recent codes such as *Synthesizer* (C. C. Lovell et al. 2025; W. J. Roper et al. 2026; T. Harvey et al. 2026), *PyMGAL* (P. Janulewicz & W. Cui 2025), and *FORECAST* (F. Fortuni et al. 2023). Briefly speaking, these methods assign spectral energy distributions (SEDs) directly to star particles based on their stellar masses, ages, and

metallicities, subsequently applying dust attenuation prescriptions and summing the contributions to produce synthetic galaxy imaging and spectra data cubes.

While this approach may sacrifice some of the geometric complexity captured by full radiative transfer, it offers significant advantages in terms of computational efficiency and methodological flexibility. Particle-based spectral modeling enables rapid generation of synthetic observations for large galaxy samples, making it particularly suitable for population studies and statistical analyses of galaxy properties. With this flexibility and efficiency, this tool could be used to thoroughly study the impact of specific choices in forward modeling on the resulting observational properties.

The particle-based spectral modeling approach, as implemented in our newly developed *GalSyn* (Galaxy Synthesizer) package, provides a comprehensive control over each physical process involved in the synthesis procedure. Users can select from multiple stellar population synthesis models, customize isochrone grids and spectral libraries, experiment with different initial mass functions, and implement flexible dust attenuation laws. This comprehensive control over the physical modeling enables detailed experimentation with various combinations of assumptions and prescriptions. This also enables data-driven Bayesian model selection across a range of use cases, allowing us to relax traditionally held assumptions.

Such flexibility is crucial for advancing our understanding of galaxy evolution in several ways. First, it enables systematic exploration of degeneracies among different physical processes and their observational signatures. This can be done, such as by studying the effects of varying physical models on the observational properties. Second, it enables optimization studies aimed at identifying the combination of physical models that best reproduce observed galaxy properties. Third, it facilitates the development and testing of new theoretical prescriptions within a consistent framework. This capability is particularly valuable for identifying optimal configurations of physical models that can generate synthetic observations, whether broadband images or integral field unit (IFU) spectroscopic data, that closely match real observational datasets.

In this paper, which is the first in a series, we describe the forward-modeling algorithms implemented in *GalSyn* and demonstrate its robustness and core capabilities. We also present the initial release of synthetic data cubes generated from the IllustrisTNG simulation suites (D. Nelson et al. 2018, 2019a; F. Marinacci et al. 2018; J. P. Naiman et al. 2018; V. Springel et al. 2018; A. Pillepich et al. 2018, 2019; D. Nelson et al. 2019b).

This release includes four mock survey fields covering areas of 5 (TNG50-1), 8 (TNG50-1), 137 (TNG100-1), and 365 (TNG300-1) arcmin², imaging data cubes of individual galaxies within those fields, and data cubes for two specific TNG50 samples: progenitors of local massive galaxies ($\log(M_*/M_\odot) > 10.5$) and 200 major-merger systems. Each data cube of a galaxy contains imaging data in multiple filters (HST, JWST, Roman, LSST, and Euclid) and a wide range of physical property maps. A forthcoming paper will provide a comprehensive exploration of how various dust attenuation laws impact observable properties.

This paper is structured as follows. In Section 2, we describe the `GalSyn` design and physical ingredients within it. Subsequently, in Section 3, we describe the data products and further processing of the data cubes by adding observational effects. The first set of data release is presented in Section 4, while the summary and outlook are given in Section 5.

2. GalSyn DESIGN

`GalSyn` is designed with a modular structure, allowing flexible customization of modeling ingredients. The overall analysis workflow of `GalSyn` is described below.

2.1. Preparation Stage

2.1.1. Input Simulation Data

The first step in the `GalSyn` workflow is the preparation of the input simulation data. `GalSyn` is designed to be agnostic to the specific hydrodynamical simulation data used, enabling its application to a wide range of simulations such as IllustrisTNG (D. Nelson et al. 2019a), EAGLE (J. Schaye et al. 2015), and others. This flexibility is achieved by first converting the raw simulation output into a standardized HDF5 file format, which serves as the input for all subsequent synthesis tasks. This step ensures that the core `GalSyn` routines operate on a consistent data structure, regardless of the data’s origin.

The resulting standardized file must contain the datasets listed in Table 1, including the coordinates, velocities, and physical properties (e.g., mass and metallicity) of the star and gas particles. Some of the gas parameters are derivable from the other parameters. The gas temperature can be derived from the internal energy and electron abundance. The hydrogen mass can be derived from the total gas mass assuming a constant hydrogen fraction (X_H). The instantaneous SFR is calculated from the gas cell by dividing the cell’s estimated cold-phase mass by a density-dependent star formation timescale once a certain density threshold is exceeded. In IllustrisTNG, this threshold is $\simeq 0.1 \text{ cm}^{-3}$.

The `simutils_tng` module provides a streamlined set of tools for handling data from the IllustrisTNG simulation. The procedure involves two main steps: data acquisition with functions for downloading a cutout for a specific subhalo or parent halo at a given snapshot, and conversion to a standardized data format that includes the necessary unit conversion and calculations to transform the data into the physical units required by `GalSyn`. New modules for handling data from other simulations will be added to `GalSyn` in future updates.

2.1.2. SSP and Nebular Emission Grids

The foundational element of the light synthesis in `GalSyn` is the assignment of a Simple Stellar Population (SSP) spectrum, including nebular emissions, to each star particle. `GalSyn` offers a highly flexible framework for this process, allowing users to either generate SSPs on-the-fly or, for significantly improved computational efficiency, use pre-computed grids of SSP models. These pre-computed grids, which store spectra across a range of ages, metallicities, and ionization parameters (U), can be generated using dedicated modules (`ssp_generator_fsps` and `ssp_generator_bagpipes`). The ionization parameter, which describes the intensity of the ionizing radiation field relative to the density of the gas, is a parameter controlling the nebular emission component.

`GalSyn` provides two options for SPS codes: the Flexible Stellar Population Synthesis (FSPS; C. Conroy et al. 2009; C. Conroy & J. E. Gunn 2010) and `bagpipes` (A. C. Carnall et al. 2018). When using FSPS, users can customize a wide array of model components, including the choice of stellar isochrones (MIST, J. Choi et al. 2016; Padova, L. Girardi et al. 2000; PARSEC, A. Bressan et al. 2012; BaSTI, A. Pietrinferni et al. 2004; and Geneva, G. Schaller et al. 1992), stellar spectral libraries (MILES, P. Sánchez-Blázquez et al. (2006), and BaSeL, T. Lejeune et al. 1997), and a comprehensive selection of Initial Mass Functions (IMFs), including E. E. Salpeter (1955), G. Chabrier (2003), P. Kroupa (2001), P. G. van Dokkum (2008), R. Davé (2008), and tabulated piece-wise power law IMF (specified in `imf.dat` file in FSPS data directory). Furthermore, FSPS implementation includes the option of the BPASS model J. J. Eldridge et al. (2017), which incorporates the effects of binary stellar evolution. Additionally, `GalSyn` also provides the 2016 version of the G. Bruzual & S. Charlot (2003) isochrones called through `bagpipes`. This implements P. Kroupa & C. M. Boily (2002) IMF.

By providing access to these different SPS engines and their various internal model choices, `GalSyn` serves as a powerful laboratory. This flexibility allows us to sys-

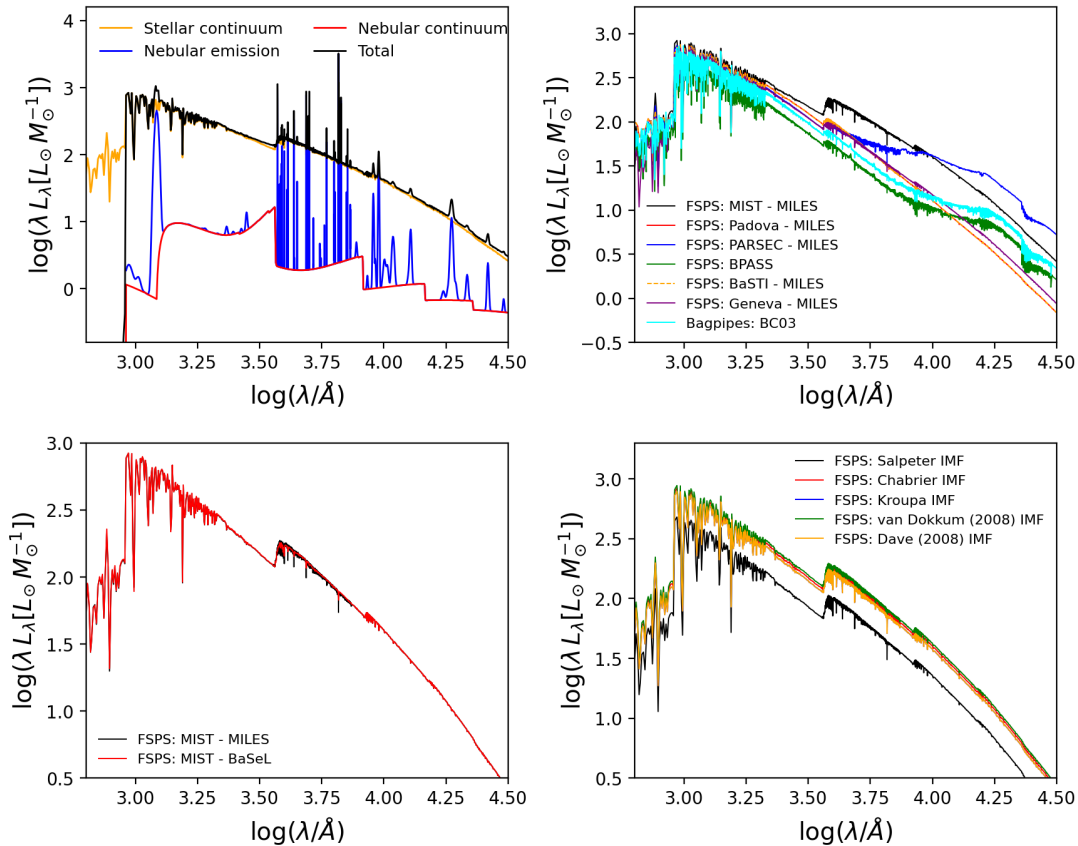


Figure 1. Comparisons of SSP spectra available in `GalSyn`. *Top left:* an example of SSP spectrum broken down into its components: stellar continuum, nebular continuum, and nebular emission. *Top right:* comparison of SSP spectra for various isochrones using the MILES spectral library and G. Chabrier (2003) IMF, calculated using the FSPS code. A BC03 spectrum generated with the Bagpipes code is also shown for reference. *Bottom left:* comparison of SSP spectra for different spectral libraries, but the same isochrone (MIST) and IMF (G. Chabrier 2003). *Bottom right:* SSP spectra with various IMFs, but the same isochrone (MIST) and spectral library (MILES).

tematically investigate how different assumptions about stellar evolution and atmospheres impact the emergent light from galaxies. The resulting SSP spectra are normalized to $1 M_{\odot}$, with the surviving stellar mass recorded in the output HDF5 file. During the synthesis process, the ratio between this surviving mass and the mass of the star particles is used to correctly scale the final spectra.

`GalSyn`'s nebular emission modeling is physically coupled to the young stellar populations (with age below 10 Myr) whose ionizing photon production is intrinsically calculated by the chosen SPS code (either FSPS or `bagpipes`). Both codes use the photoionization code `CLOUDY` (G. J. Ferland et al. 1998, 2013) to self-consistently model the resulting nebular continuum and emission lines. There are generally two parameters in the nebular emission modeling: U and gas-phase metallicity. While FSPS treats gas-phase metallicity as an independent parameter, `bagpipes` inherently ties it to have the same value as the stellar metallicity. To

maintain computational efficiency in FSPS without introducing an additional free parameter (which will add a dimension in SSP grids), we allow users to tie the gas-phase metallicity to the stellar metallicity using a fixed input ratio. The calculation of U from simulation data is described in Section 2.2.2.

2.2. Synthesis Process

The `GalSyn` synthesis pipeline begins by performing a spatial projection, transforming the 3D coordinates of star and gas particles from a simulation into a 2D image plane based on a specified viewing angle. The core of the synthesis is then executed in parallel (employing multiple CPUs) for each pixel. The initial pixel size (i.e., sampling) is defined by the input smoothing length, which is assumed constant. For every star particle within a pixel's line-of-sight, the code assigns an SSP spectrum, applies a kinematic Doppler shift based on particle velocities, and models dust attenuation from both the diffuse interstellar medium and the local birth

Table 1. List of Physical Parameters in the Standardized Input Simulation Data

Parameter	Description	Units
Properties for both Star and Gas Particles		
<code>coords</code>	3D particle positions	kpc
<code>vel</code>	3D particle velocities	km/s
<code>mass</code>	Particle mass (surviving mass for stars)	M_{\odot}
<code>zmet</code>	Particle metallicity (mass fraction)	Dimensionless
Star-Specific Properties		
<code>init_mass</code>	Stellar mass at the time of formation	M_{\odot}
<code>form_z</code>	Redshift at which the star particle formed	
Gas-Specific Properties		
<code>sfr_inst</code>	Instantaneous star formation rate	M_{\odot}/yr
<code>temp</code>	Gas temperature	Kelvin
<code>mass_H</code>	Hydrogen mass of the gas particle	M_{\odot}

Table 2. Stellar Population Synthesis (SPS) Modeling Options in GalSyn

Model Component	FSPS Options	Bagpipes Options
SPS Engine	Flexible Python wrapper for the Fortran FSPS code. (Conroy et al. 2009; Conroy & Gunn 2010)	Built upon the Bruzual & Charlot (2003) models. (Carnall et al. 2018)
Isochrones Spectral Library	MIST, BaSTI, Padova, PARSEC, Geneva MILES, BaSeL	Bruzual & Charlot (2003) models
Initial Mass Function (IMF)	Chabrier (2003), Kroupa (2001), Salpeter (1955), Custom power-law, van Dokkum (2008), Dave (2008)	Kroupa (2001)
Binary Evolution	BPASS models can be integrated.	Not included by default.

cloud. The light from all particles in the pixel is then aggregated, and the final spectrum is redshifted, attenuated by the intergalactic medium (IGM), and integrated through user-defined filter transmission functions to produce the observed broadband flux. Finally, the synthetic cube is regridded into the user-desired pixel scale.

2.2.1. Spatial Projection

The first step in the synthesis process is to transform the three-dimensional distribution of star and gas particles from the simulation into a two-dimensional image plane that represents the observer’s view. This process constructs the viewing geometry, projects the particles, and calculates their positions along the line of sight.

The viewing orientation is defined by two key parameters: the polar angle and the azimuth angle. These angles specify the observer’s position in a spherical coordinate system centered on the galaxy. The polar angle controls the inclination, representing a tilt from the simulation’s z-axis, while the azimuth angle controls the

rotation of the galaxy in the xy-plane. Based on these angles, the code constructs a rotation matrix that transforms the original (x, y, z) coordinates of every particle into a new coordinate system (x’, y’, z’). In this new frame, the z’-axis is aligned with the observer’s line of sight (LOS), and the x’-y’ plane represents the plane of the sky.

After this transformation, the (x’, y’) coordinates of each particle are used to bin them into a 2D pixel grid, forming the basis of the final image. The initial pixel grid is set by the input smoothing length (`smoothing_length`), which can be thought of as the spatial resolution of the simulation. The z’ coordinate of each particle becomes its distance along the line of sight. A crucial calculation is performed at this stage: the code determines the minimum z’ value among all particles (both stars and gas) and normalizes all z’ distances relative to this minimum. This results in a relative line-of-sight distance for every particle, where a value of 0 corresponds to the particle closest to the ob-

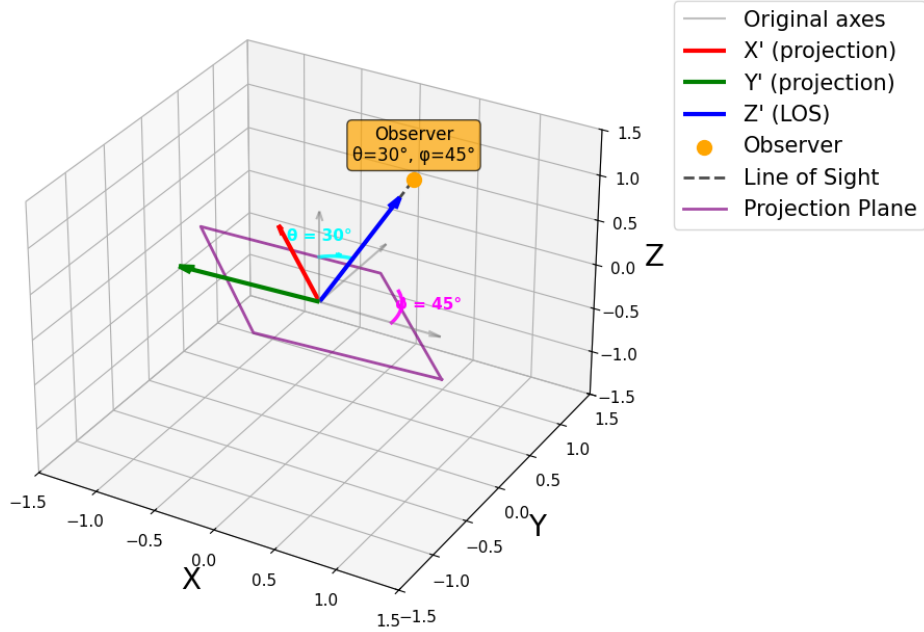


Figure 2. Visualization of two-dimensional projection from three-dimensional coordinates given a viewing angle specified by the polar (θ) and azimuth angles (ϕ). The new coordinate system (x' , y' , z') obtained from the transformation is shown by the red, green, and blue arrows. In this new frame, the observer’s LOS is aligned with the z' -axis, and the x' - y' plane represents the plane of the sky.

server. This relative distance is essential for the subsequent dust attenuation modeling (to be described in Section 2.2.5), as it allows the code to robustly identify which gas particles are physically located *in front of* any given star particle, and thus contribute to the attenuation of its light.

The central coordinate of the synthetic cutout is determined through a two-pass procedure. In the first pass, all star particles are projected onto a preliminary 2D pixel grid spanning the full extent of the simulation data, using the same rotation matrix described above. A stellar mass density map is then constructed by accumulating the mass of each star particle into its corresponding pixel. The pixel containing the highest total stellar mass is identified as the galaxy center, and its physical coordinate in the projected plane is taken as the central reference point. In the second pass, the final cutout grid is defined such that this most-massive pixel lies at the geometric center of the output image, with the cutout dimensions set by the user-specified output size. The physical size of the cutout can either be specified directly by the user in kpc, or determined automatically as the smallest square that encloses a user-defined fraction of the total projected stellar mass (default: 99%).

2.2.2. Calculation of Ionization Parameter

To account for the local physical conditions of the ISM in simulated galaxy into the nebular emission modeling,

we calculate the ionization parameter (U) for each pixel. For an ionization-bounded H II region, U can be calculated as

$$U = \frac{Q}{4\pi R^2 n_{\text{H}} c}, \quad (1)$$

where Q , n_{H} , R , and c are the hydrogen-ionizing photon production rate, hydrogen number density, characteristic size of the H II region, and the speed of light, respectively (e.g., N. A. Reddy et al. 2023a,b). The radius can be approximated as the Strömgen radius:

$$R_S = \left(\frac{3Q}{4\pi\alpha_B n_{\text{H}}^2 \epsilon} \right)^{1/3}, \quad (2)$$

where α_B is the case-B recombination coefficient and ϵ is the volume filling factor. Here, we assume fully ionized gas ($n_{\text{H}} \approx n_e$, electron density) for simplicity. Substituting radius in Equation 1 with R_S , we obtain

$$U = k (n_{\text{H}} Q \epsilon^2)^{1/3} \quad (3)$$

with $k = \left(\frac{3\alpha_B^2}{16\pi c^3} \right)^{1/3}$. Assuming $\alpha_B = 2.59 \times 10^{-13} \text{ cm}^3 \text{ s}^{-1}$ for temperature of $T = 10^4 \text{ K}$, we obtain $k = 5.3 \times 10^{-20} \text{ cm s}^{1/3}$.

The production rate of hydrogen-ionizing photons can be calculated via

$$Q = \xi_{\text{ion}} L_{\text{UV}}, \quad (4)$$

where ξ_{ion} is the ionizing photon production efficiency and L_{UV} is the ultraviolet (UV) luminosity. ξ_{ion} is a free parameter with a default value of $10^{25.39} \text{ erg}^{-1} \text{ Hz}$, while L_{UV} is calculated from pixel’s instantaneous SFR assuming [R. C. Kennicutt \(1998\)](#).

The calculated U is clipped to a standard physical range of 10^{-4} to 10^{-1} . The derived U of a pixel is then used in assigning spectra of stellar particles in the pixel (to be described in [Section 2.2.3](#)). This approach allows the ionization state of the gas to vary spatially across the simulated galaxy, self-consistently reflecting the relationship between local star formation feedback and the surrounding gas density.

2.2.3. Spectra Assignment

The core of `GalSyn`’s light generation is assigning an SSP spectrum to each star particle based on its age, metallicity, ionization parameter, and mass. This is handled in one of two ways, with the goal of obtaining two separate spectral components: the stellar continuum and the nebular emission.

- Method 1: Using a pre-computed SSP grid. This is the fastest, default method. The code reads from an HDF5 file containing a pre-calculated grid of spectra. For each star particle, it uses the particle’s age, metallicity, and ionization parameter (of the pixel where the particle resides) to locate the corresponding entry in the SSP grid. The spectrum is then obtained by interpolating between grid points using one of three supported techniques: `linear`, `nearest`, or `cubic`. Interpolation is applied consistently to both the stellar continuum and nebular emission components of the star particle. Finally, the interpolated spectra are rescaled by the particle’s mass. The robustness of the interpolation methods are tested and discussed in [Appendix A](#).
- Method 2: On-the-fly SSP generation. In this mode, an SSP instance (either `FSPS` or `bagpipes`) is initialized for each parallel worker and configured with the star particle’s specific age, metallicity, and ionization parameter. To isolate the nebular emission, the SSP model is run twice: once with nebular emission enabled to get a total spectrum, and a second time with it disabled to get the stellar continuum only. The final nebular spectrum is then obtained by subtracting the stellar-only from the total spectrum, resulting in two spectral components for each star particle.

2.2.4. Kinematic Effects

`GalSyn` includes a treatment of galaxy kinematics, which is designed to realistically model the distinct motions of stellar populations and the interstellar medium (ISM). Rather than assuming that ionized gas moves with the stars that excite it, the code implements a decoupled kinematics model. This ensures that the stellar and nebular components of a star particle’s spectrum are Doppler-shifted independently, reflecting their different physical origins.

The stellar continuum, which represents the integrated light from the stars themselves, is shifted based on the line-of-sight velocity of its parent star particle. This directly ties the stellar absorption features in the final spectrum to the underlying stellar dynamics of the simulated galaxy.

In contrast, the nebular emission spectrum is shifted according to the light-weighted average line-of-sight velocity of the local gas particles. These are identified by applying the following criteria. For each star particle, the code searches for nearby gas particles that are located physically within a close 3D physical distance defined by `max_dist_neb` (with a default value of 500 pc) of the star particle and having positive instantaneous SFR.

This procedure ensures that the emission lines in the final spectrum trace the kinematics of the local ISM, while the stellar absorption features trace the stellar kinematics. This decoupling is essential for creating realistic synthetic Integral Field Unit (IFU) data, as it allows for the independent measurement and analysis of gas and stellar rotation curves, a critical technique in observational studies of galaxy dynamics.

2.2.5. Dust Attenuation

Dust is an important component of galaxies, even though it typically accounts for only $\sim 1\%$ of the total ISM mass (e.g., [M. G. Edmunds 2001](#); [B. T. Draine 2003](#)). It influences various physical processes in the ISM, such as facilitating the formation of molecular hydrogen on grain surfaces (e.g., [D. Hollenbach & E. E. Salpeter 1971](#); [D. Hollenbach & C. F. McKee 1979](#)), and creating conditions favorable for star formation (e.g., [B. T. Draine 2003](#); [M. R. Krumholz et al. 2009](#)). Dust also affects stellar light by scattering and absorbing it, then re-emitting the energy in the infrared as thermal radiation (e.g., [E. da Cunha et al. 2008](#)).

`GalSyn` aims to realistically model both the production and processing of light in galaxies; therefore, incorporating dust effects is essential. In the current version of `GalSyn`, however, we only include dust attenuation and omit dust emission, as the main goal of the code is

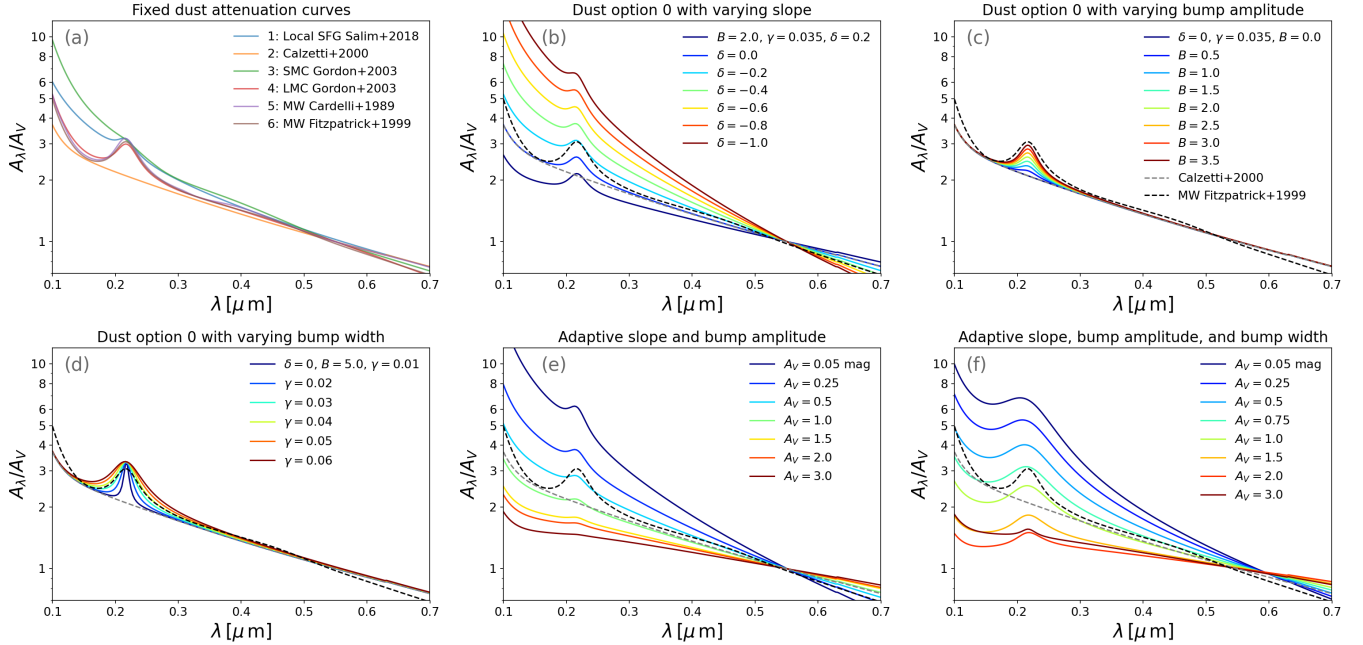


Figure 3. Options for the dust attenuation curves of the diffuse ISM in `GalSyn`. (a) The fixed dust attenuation law options: S. Salim et al. (2018), D. Calzetti et al. (2000), SMC by K. D. Gordon et al. (2003), LMC by K. D. Gordon et al. (2003), MW by J. A. Cardelli et al. (1989), and MW by E. L. Fitzpatrick (1999). These dust curves have a fixed shape, independent of the local A_V . (b) The modified Calzetti law (option 0), as defined in Equations 8-9. This model is shown with a varying slope (δ) and fixed UV bump parameters ($B = 2.0$ and $\gamma = 0.035$). (c) The modified Calzetti law shown with a varying bump amplitude but fixed slope ($\delta = 0$) and bump width ($\gamma = 0.035 \mu\text{m}$). (d) The modified Calzetti law shown with a varying bump width but fixed slope ($\delta = 0$) and bump amplitude ($B = 5$). (e) The modified Calzetti law is applied in an adaptive mode with slope and bump amplitude changes depending on A_V . The slope varies with A_V following the empirical relation from S. Salim et al. (2018), and the bump amplitude then varies depending on slope following the relation from M. Kriek & C. Conroy (2013). (f) Dust attenuation curve obtained by fitting modified Calzetti law to the integrated A_λ curves from synthetic IFS cubes of simulated galaxies from the NIHAO-SKIRT catalog (N. Faucher et al. 2023). Details about this will be presented in Abdurro’uf et al. (in prep.).

to generate spectrophotometric data cubes covering the rest-frame ultraviolet to near-infrared ($\sim 0.05 - 2 \mu\text{m}$), where dust emission has a negligible impact. Inclusion of dust emission is deferred to future work.

Most current hydrodynamical simulations (e.g., IllustrisTNG, EAGLE) do not explicitly track dust as a separate component. Instead, dust properties in galaxies can be inferred from the properties of gas particles. The core of dust attenuation modeling involves estimating the total extinction experienced by starlight and determining its wavelength dependence. To this end, `GalSyn` provides two distinct modeling approaches for assigning the level of dust attenuation on spatially resolved scales.

The first method (hereafter called “line-of-sight” or LOS) is based on the column density of intervening gas particles positioned along the line of sight to each star particle. In this approach, attenuation is applied individually to the spectrum of each star particle. The second option (hereafter called “sfr- A_V ”) determines the A_V for a given pixel based on the instantaneous SFR surface density of the gas cells within that pixel. This

A_V value is then applied uniformly to all star particles contributing to that pixel. This latter option is inspired by empirical correlations between SFR (or SFR density) and A_V (e.g., I. Smail et al. 2021), providing users with a simple yet physically motivated alternative for dust modeling. As shown by L. Sommovigo et al. (2025), a correlation between A_V and SFR surface density naturally emerged from radiative transfer post-processing of TNG galaxies. The specific correlation can be input by the user in the form of a dictionary (`av_sfrden_relation`). In the following, we will describe the LOS method.

In the LOS method, we model spatially resolved dust attenuation for each stellar particle by estimating the dust optical depth of the surrounding gas. We also include additional attenuation from birth clouds that affects young stars. The implementation of our dust attenuation model is described in detail below. Our approach is similar to the methods in M. Vogelsberger et al. (2020) (model B) and D. Nelson et al. (2018) (model C), but with added flexibility in several aspects, including the

choices for dust attenuation (and extinction) models. In the following, we first describe the attenuation modeling for the diffuse ISM, and then for the birth clouds.

The core of the dust model is estimating the amount of dust that starlight must pass through, which is calculated dynamically for each star particle. For a given star particle, the code identifies all gas particles in front of it along the line of sight. Only “cold” gas is selected (i.e., gas with a nonzero instantaneous SFR and a temperature below 8000 K), as this is where dust is expected to reside.

The hydrogen column density (N_{H}), which is a direct proxy for the amount of intervening material, is then computed by summing the hydrogen mass of all foreground cold gas particles and dividing it by the pixel’s physical area. With this and the gas-phase metallicity (Z_{g}), we can then estimate the V -band resolved optical depth for the stellar particle via

$$\tau_{\text{V,ISM}} = \tau_{\text{dust}}(z) \left(\frac{Z_{\text{g}}}{Z_{\odot}} \right)^{\gamma} \left(\frac{N_{\text{H}}}{N_{\text{H},0}} \right), \quad (5)$$

where $\gamma = 1$, $N_{\text{H},0} = 2.1 \times 10^{21} \text{ cm}^{-2}$, and $\tau_{\text{dust}}(z)$ (`scale_dust_tau`) is a redshift-dependent scale factor of the optical depth. This implies that the V -band optical depth is assumed to be linearly dependent on the metal mass in the galaxy disc (e.g., [R. S. Somerville et al. 2012](#); [L. Y. A. Yung et al. 2019](#)) and the redshift-dependent scale factor scales like the average dust-to-metal ratio. The $\tau_{\text{dust}}(z)$ function in `GalSyn` is easily customizable, with the default implementation following that of [M. Vogelsberger et al. \(2020, Table 3 therein\)](#).

Next, we convert the optical depth into the more commonly used V -band ($0.55 \mu\text{m}$) attenuation (A_{V}) using the relation derived from a dust-star geometry model in which ionized gas and dust are co-spatial and uniformly mixed ([D. Calzetti et al. 1994](#); [M. Vogelsberger et al. 2020](#)):

$$A_{\text{V}} = -2.5 \log \left(\frac{1 - e^{-\tau_{\text{V}}}}{\tau_{\text{V}}} \right). \quad (6)$$

Here, τ_{V} should be interpreted as an effective optical depth that accounts for both dust absorption and scattering, including photons scattered into the line of sight. Accordingly, we treat this quantity as attenuation rather than extinction.

The A_{V} value provides the overall normalization of dust attenuation, but a functional form is still required to describe how attenuation varies with wavelength (i.e., the dust attenuation curve). In principle, the shape of this curve depends on the physical properties of the dust, such as its spatial distribution, density, grain size distribution, and chemical composition. However, in the

absence of detailed knowledge of these quantities, an assumed attenuation curve needs to be adopted.

In `GalSyn`, we provide a suite of empirical dust attenuation laws commonly used in galaxy SED modeling. Additionally, we include an analytical attenuation curve extracted from SKIRT synthetic data, which is expected to serve as a representative global attenuation model derived from the radiative transfer simulation. The details of this extraction process will be described in a forthcoming paper ([Abdurro’uf et al., in prep.](#)). Within `GalSyn`, these dust attenuation curves are broadly classified into two categories: fixed and adaptive.

The fixed dust law has an unchanging shape, independent of the local A_{V} . This includes the commonly used empirical law, such as the Milky Way (MW) extinction law (e.g., [J. A. Cardelli et al. 1989](#); [E. L. Fitzpatrick 1999](#)), the Small Magellanic Cloud (SMC) extinction law (e.g., [M. L. Prevot et al. 1984](#); [K. D. Gordon et al. 2003](#)), the Large Magellanic Cloud (LMC) extinction law (e.g., [K. Nandy et al. 1981](#); [G. C. Clayton & P. G. Martin 1985](#); [K. D. Gordon et al. 2003](#)), the [D. Calzetti et al. \(2000\)](#) dust attenuation law, and the [S. Salim et al. \(2018\)](#) law, as well as the modified [D. Calzetti et al. \(2000\)](#) law with fixed parameters, explained below.

In the adaptive dust category, the shape of the dust attenuation curve is adaptive to the amount of dust attenuation (A_{V}), which allows the attenuation curve to be steeper (i.e., more UV extinction) in regions with less dust and vice versa, as expected from the observations (e.g., [S. Noll et al. 2009](#); [M. Kriek & C. Conroy 2013](#); [J. Chevallard et al. 2013](#); [B. Salmon et al. 2016](#); [S. Salim et al. 2018](#); [S. Salim & D. Narayanan 2020](#); [G. Nagaraj et al. 2022](#)). The baseline of this attenuation curve is the [D. Calzetti et al. \(2000\)](#) dust law, which is modified with a variable power-law slope and the addition of a UV bump ([S. Noll et al. 2009](#)). The original [D. Calzetti et al. \(2000\)](#) reddening curve is a piecewise function defined as:

$$k'(\lambda) = 4.05 + 2.659 \begin{cases} (-2.156 + \frac{1.509}{\lambda} - \frac{0.198}{\lambda^2} + \frac{0.011}{\lambda^3}) & \text{for } 0.12 \leq \lambda < 0.63 \mu\text{m} \\ (-1.857 + \frac{1.040}{\lambda}) & \text{for } 0.63 \leq \lambda \leq 2.20 \mu\text{m}. \end{cases} \quad (7)$$

The modified attenuation curve follows the prescription of [M. Kriek & C. Conroy \(2013\)](#):

$$\frac{A(\lambda)}{A_{\text{V}}} = \frac{k'(\lambda) + D(\lambda)}{4.05} \left(\frac{\lambda}{\lambda_{\text{V}}} \right)^{\delta} \quad (8)$$

where $\lambda_V = 0.55 \mu\text{m}$. Here, δ represents the power-law slope modification (`dust_index`), and $D(\lambda)$ is a Lorentzian-like Drude profile describing the UV bump feature at 2175\AA :

$$D(\lambda) = \frac{B(\lambda\gamma)^2}{(\lambda^2 - \lambda_0^2)^2 + (\lambda\gamma)^2} \quad (9)$$

with λ in microns, B the bump amplitude (`bump_amp`), $\lambda_0 = 0.2175 \mu\text{m}$ the central wavelength of the bump, and γ the bump width (full width at half maximum, FWHM, `bump_dwave`). While the bump width is commonly fixed at the empirical value of $0.035 \mu\text{m}$ (S. Noll et al. 2009), we make it a free parameter in `GalSyn`. As will be shown in Abdurro'uf et al. (in prep.), the bump width is inversely correlated with A_V in SKIRT RT simulation.

The three parameters of the modified D. Calzetti et al. (2000) dust curve (δ , B , and γ) are fully customizable within `GalSyn`. Users may choose to hold these parameters constant at specific values or define them as functions of A_V by providing the desired correlations in the form of a dictionary. This flexibility allows us to mimic empirical dust attenuation trends, such as the observed correlation between the power-law slope and A_V (e.g., S. Salim et al. 2018; G. Nagaraj et al. 2022; A. J. Battisti et al. 2020) or the relationship between the UV bump amplitude and the power-law slope, such as $B = 0.85 - 1.9\delta$ reported by M. Kriek & C. Conroy (2013).

Below, we list the dust attenuation law options (`dust_law`) in `GalSyn`:

- Option 0: The modified Calzetti law as detailed above. The three parameters (`dust_index`, `bump_amp`, and `bump_dwave`) can be fixed at user-defined values or configured to depend on A_V by supplying the desired correlations in the form of a dictionary.
- Option 1: The S. Salim et al. (2018) attenuation law.
- Option 2: The original D. Calzetti et al. (2000) law.
- Option 3: The SMC extinction law from K. D. Gordon et al. (2003).
- Option 4: The LMC extinction law from K. D. Gordon et al. (2003).
- Option 5: The MW extinction law from J. A. Cardelli et al. (1989).

- Option 6: The MW extinction law from E. L. Fitzpatrick (1999).

The S. Salim et al. (2018) dust attenuation law uses a custom polynomial reddening curve $k(\lambda)$ combined with the Drude profile:

$$A(\lambda) = \frac{A_V k(\lambda)}{R_V}. \quad (10)$$

The reddening curve $k(\lambda)$ is defined as:

$$k(\lambda) = a_0 + \frac{a_1}{\lambda} + \frac{a_2}{\lambda^2} + \frac{a_3}{\lambda^3} + D(\lambda, B) + R_V, \quad (11)$$

where a_0 , a_1 , a_2 , and a_3 are the polynomial coefficients (`salim_a0` to `salim_a3`), D is the Drude profile with bump strength B (`salim_B`), and R_V is the total-to-selective extinction ratio (`salim_RV`).

To illustrate the variation in the shape of the dust attenuation curves provided in `GalSyn`, we present them in Figure 3. In Abdurro'uf et al. (in prep.), we derive a global dust attenuation law from radiative transfer simulations using synthetic spectroscopic data cubes from the NIHAO-SKIRT catalog (N. Faucher et al. 2023). These data were generated using the SKIRT code. We fitted the integrated dust attenuation curves using the modified Calzetti formula described above. Our results indicate that all the primary parameters (slope, bump amplitude, and bump width) correlate strongly with A_V . Specifically, as A_V increases, the slope increases, while both the bump amplitude and width decrease. The resulting curve is shown in the bottom right panel (f). This attenuation curve can be easily implemented in `GalSyn` using option 0.

Finally, the LOS method accounts for the extra attenuation for young stars with an age less than a specified value (`t_esc`), typically 10 Myr. The shape of this curve is defined as a simple power law of

$$A(\lambda) = A_{V,BC} \left(\frac{\lambda}{\lambda_V} \right)^{\delta_{BC}} \quad (12)$$

with $A_{V,BC}$ is the V -band attenuation from the birth clouds and δ_{BC} is a power-law slope. The $A_{V,BC}$ can be set to relate with the A_V of the diffuse ISM through η (`dust_eta`), defined as $\equiv A_{V,BC}/A_V$. The δ_{BC} is a free parameter with a default of -0.7 .

2.2.6. Cosmological Redshifting

Up to this point, the synthetic pixel spectra are in the rest frame of the galaxy. To transform them into observable quantities, we apply a cosmological redshifting. This process accounts for the expansion of the Universe, which both stretches the wavelength of light and

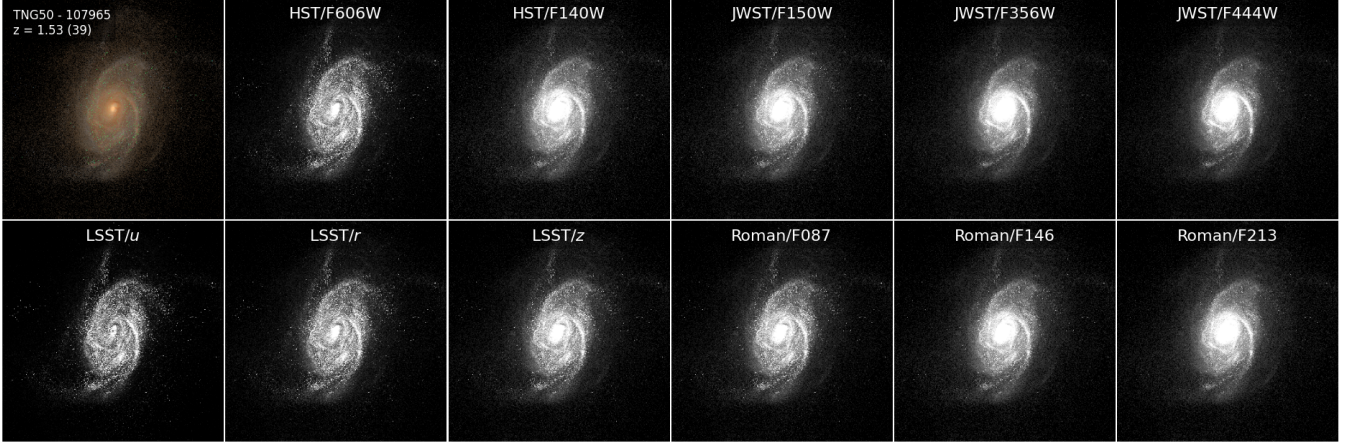


Figure 4. Example of synthetic images of a simulated galaxy from TNG50 (subhalo ID=107965) at $z = 1.53$ across multiple filters from various telescopes, including HST, JWST, Rubin/LSST, and Roman Space Telescope. The top-left panel shows a color composite image generated from JWST filters: F115W (blue), F150W (green), and F200W (red). These images have a pixel size of 0.03 arcsec^{-1} and have no observational effects being added.

diminishes its observed flux. The rest-frame spectrum, with luminosity density L_λ in units of $L_\odot \text{ \AA}^{-1}$ is converted to an observed-frame flux density, F_λ in units of $\text{erg s}^{-1} \text{ cm}^{-2} \text{ \AA}^{-1}$. The transformation is based on the galaxy’s redshift, z , and the luminosity distance, $D_L(z)$, as determined by the chosen cosmology. The observed wavelength is calculated as $\lambda_{\text{obs}} = \lambda_{\text{rest}}(1+z)$, while the corresponding observed flux density is given by:

$$F_\lambda(\lambda_{\text{obs}}) = \frac{L_\lambda(\lambda_{\text{rest}})}{4\pi D_L(z)^2(1+z)}. \quad (13)$$

2.2.7. IGM absorption

As light from a distant galaxy travels to an observer, it passes through the Intergalactic Medium (IGM), where intervening clouds of neutral hydrogen absorb photons, primarily at ultraviolet wavelengths. This effect is crucial for accurately modeling the observed spectra of high-redshift galaxies. `GalSyn` applies this absorption to the final, redshifted spectrum of each pixel. The final observed flux is the product of the intrinsic flux and the IGM transmission, $T_{\text{IGM}}(\lambda, z)$:

$$F_{\lambda, \text{obs}}(\lambda) = F_{\text{int}}(\lambda) T_{\text{IGM}}(\lambda, z). \quad (14)$$

`GalSyn` provides two widely-used empirical models for calculating the IGM transmission: P. Madau (1995) and A. K. Inoue et al. (2014).

2.2.8. Integrating Through Filter Transmission Functions

To transform the synthesized spectra into observable photometric fluxes, we simulate the process of observing the object through a set of standard astronomical filters. The average flux density from a given spectrum

$F_\lambda(\lambda)$ that is observed through a filter with a transmission function of $T(\lambda)$ can be computed using the following equation:

$$\langle F_\lambda \rangle = \frac{\int F_\lambda(\lambda) T(\lambda) \lambda d\lambda}{\int T(\lambda) \lambda d\lambda} \quad (15)$$

This calculation is performed for each pixel in the image grid and for every specified filter, yielding the final multi-band photometric data cubes. The resulting flux is in units of $\text{erg s}^{-1} \text{ cm}^{-2} \text{ \AA}^{-1}$. This flux is then converted into the user-selected units. The available options for this are: MJy/sr, nJy, AB magnitude, and $\text{erg s}^{-1} \text{ cm}^{-2} \text{ \AA}^{-1}$.

For converting the calculated flux densities between different unit options available in `GalSyn`, it is necessary to define the pivot wavelength, which can be calculated from the transmission curve using the following equation:

$$\lambda_p = \sqrt{\frac{\int T(\lambda) \lambda d\lambda}{\int \frac{T(\lambda)}{\lambda} d\lambda}}. \quad (16)$$

This calculation is only performed in the generation of the photometric datacube, and not for the IFU datacube.

2.3. Physical Property Maps Reconstruction

Beyond creating synthetic images, `GalSyn` produces a comprehensive suite of 2D physical property maps of the simulated galaxies. These maps are generated by aggregating the properties of the constituent star and gas particles that fall within the line-of-sight of each pixel. The physical property maps are derived using three primary methods:

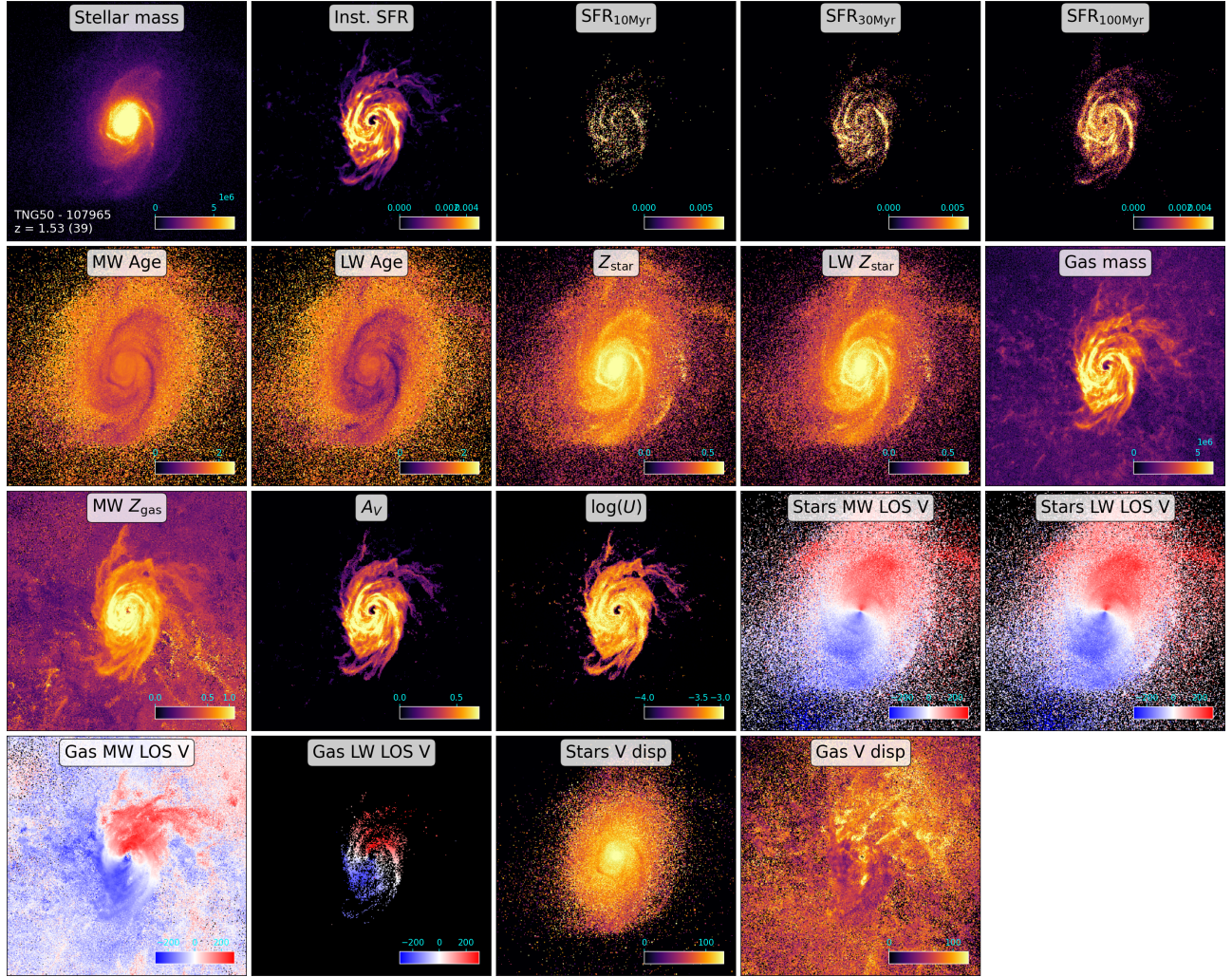


Figure 5. Spatially resolved physical property maps of the galaxy TNG50-107965, the same galaxy shown in Figure 4. These maps have the same spatial sampling as those of the synthetic images ($0.03'' \text{ pixel}^{-1}$). This illustrates the comprehensive set of physical property maps generated by GalSyn.

- **Summation:** This method involves summing a specific property from all relevant particles within a pixel. It is used for extensive quantities like total stellar or gas mass.
- **Mass-Weighted Average:** This method is employed to calculate a physically representative mean value for a property such as age or metallicity. For a given property P , the average value $\langle P \rangle_{\text{mass}}$ for a pixel containing N particles is calculated as:

$$\langle P \rangle_{\text{mass}} = \frac{\sum_{i=1}^N m_i P_i}{\sum_{i=1}^N m_i} \quad (17)$$

where m_i and P_i are the mass and property of the i -th particle, respectively. This method ensures that more massive particles, which contribute more significantly to the system's total

mass, have a proportionally larger impact on the average.

- **Light-Weighted Average:** This method is adopted to better represent what would be measured in an actual observation. This method weights each particle's contribution by its bolometric luminosity, L_i , which is calculated from its spectrum. Since young, massive stars are brighter than the old ones, this method provides an observationally-biased mean that reflects what we see in the observation. The light-weighted average, $\langle P \rangle_{\text{light}}$, is calculated as:

$$\langle P \rangle_{\text{light}} = \frac{\sum_{i=1}^N L_i P_i}{\sum_{i=1}^N L_i} \quad (18)$$

The list of generated physical property maps is given in Table 4, and an example of the maps for the galaxy TNG50-107965 is shown in Figure 5.

While an extensive analysis of property maps for a large galaxy sample is beyond the scope of this paper, we demonstrate here the robustness of the ionization parameter estimates formulated in Section 2.2.2. As shown in Figure 6, the ionization parameter correlates strongly with SFR surface density on spatially resolved scales within the galaxy TNG50-107965. This aligns well with the empirical relation derived by N. A. Reddy et al. (2023a) for star-forming galaxies at $2.7 < z < 6.3$.

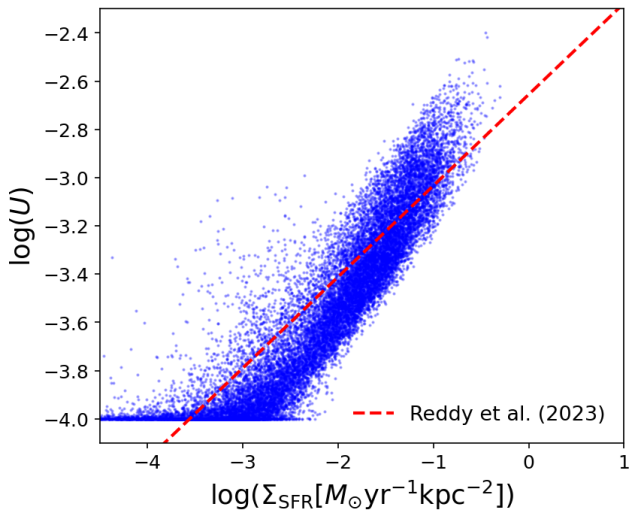


Figure 6. Correlation between the spatially resolved ionization parameter and SFR surface density in the galaxy TNG50-107965 as derived using `GalSyn` (see Figure 5). Each data point represents a single pixel of size 0.03 arcsec, corresponding to 0.26 kpc. The dashed line shows the empirical correlation from N. A. Reddy et al. (2023a). There is a good agreement between the predicted correlation from `GalSyn` and the empirical correlation. The calculated U is capped to a physical range of 10^{-4} to 10^{-1} (see Section 2.2.2), which makes the artificial cut at the bottom of the correlation.

2.4. Spatially Resolved SFH Reconstruction

To understand how different regions of a galaxy were assembled over cosmic time, `GalSyn` includes a functionality to reconstruct the spatially resolved SFH. This process analyzes the formation properties of star particles on a pixel-by-pixel basis, resulting in a comprehensive dataset that traces the growth and chemical evolution across the galaxy.

The reconstruction begins by preparing the simulation data for analysis. Essential properties, specifically the initial mass, formation time, metallicity, and 3D coordinates, are loaded for all star particles. The formation

time of each particle is converted into a lookback time from the perspective of the galaxy’s snapshot redshift. Subsequently, all star particles are projected onto a 2D pixel grid according to the specified viewing angle (see Section 2.2.1). This step generates a membership list for each pixel, detailing exactly which star particles fall within its line-of-sight.

The core of the reconstruction is performed in parallel for each pixel on the grid to ensure computational efficiency. For every pixel, the associated star particles are gathered and binned into discrete time intervals based on their lookback time, with the user-defined bin width (with a default value of 50 Myr). Within each lookback time bin, several key physical properties are calculated:

- **Mass Formed:** The sum of the initial masses of all star particles in the bin.
- **Star Formation Rate (SFR):** The total mass formed in the bin divided by the time width of the bin, yielding an average SFR in M_{\odot}/yr .
- **Mass-Weighted Metallicity:** The average metallicity of the stars in the bin, weighted by their initial mass.
- **Cumulative Mass:** The running total of all stellar mass formed up to the end of that time bin

Once the SFH is constructed for a pixel, the cumulative mass history is used to derive key stages in its formation. By interpolating the cumulative mass array, the specific lookback time at which the pixel had formed a certain percentage of its final stellar mass is determined. This is calculated for several key fractions: 5%, 10%, 25%, 50%, 75%, and 95%. These mass assembly times can provide a useful insight on whether a region of the galaxy formed its stars early and rapidly or over a more extended period.

The final output is a single, comprehensive FITS file that aggregates the results from all pixels. This includes 3D data cubes for SFR, stellar mass formed, and metallicity, with axes corresponding to the two spatial dimensions and lookback time. Additionally, the derived mass assembly times (e.g., t_{50} , t_{95}) are saved as 2D maps. These are summarized in Table 5.

2.5. Regridding to Desired Pixel Scale

As described in Section 2.2.1, the initial 3D to 2D projection is performed at a high-resolution grid based on the smoothing length of the simulation. After the synthesis process, the synthetic images and property maps are resampled to a user-defined pixel scale using a spatial resampling process that ensures physical consistency. The regridding is handled differently depending

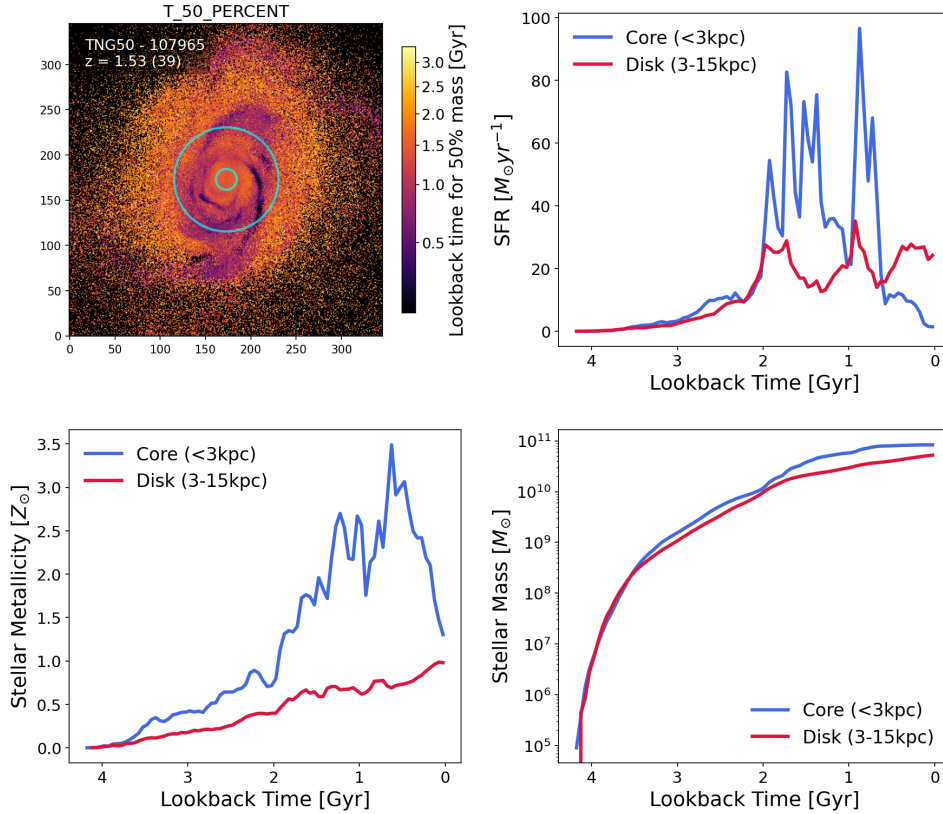


Figure 7. Spatially resolved SFH of the galaxy TNG50-107965 as reconstructed by `GalSyn`. *Top left:* the map of spatially resolved lookback time for 50% mass assembly (`T_50_PERCENT`). *Top right:* comparison between the integrated SFH of the central region ($r < 3$ kpc) and the disk ($3 < r < 15$ kpc). *Bottom left:* comparison for metallicity history. *Bottom right:* comparison for stellar mass growth history.

on the type of data being processed. For images representing physical quantities like light (flux) or mass, the resampling is performed in a flux-conserving mode. In this case, the resampling process is designed to preserve the total integrated value across the grid. This ensures that even as the spatial resolution changes, the total physical quantity represented in the data cube remains consistent.

For maps that represent average characteristics, such as the stellar age, metallicity, or velocity, the module uses an averaging mode. This process is carefully managed to only include pixels that actually contain data, preventing empty space from “diluting” or artificially lowering the physical values of the galaxy properties.

The computational cost needed for synthesizing the data cube of a galaxy depends on the number of particles (stars and gas) in the galaxy. The typical computational cost for synthesizing imaging data (in 47 filters) of a galaxy with 5×10^5 star particles and 7×10^5 gas particles is ~ 1 CPU hour¹¹.

¹¹ This is ~ 6 minutes for a parallel computation using 10 cores.

3. SYNTHETIC DATA PRODUCTS AND OBSERVATIONAL REALISM

3.1. Synthetic Data Cubes

From the synthesis processes described in the previous section, `GalSyn` produces a comprehensive set of data products. The outputs can be categorized into four main types: synthetic imaging, IFU data cubes, physical property maps, and spatially resolved SFH maps. The imaging, IFU (when requested for output) data cubes, and physical property maps are stored in a single multi-extension FITS file. The resolved SFH maps are generated via a different module, and they are stored in a single multi-extension FITS file.

The synthetic imaging and IFU data cubes contain dust-free and dust-attenuated data. The FITS file extensions for the synthetic data and the derived property maps are summarized in Table 3 and 4, respectively. The FITS file extension for resolved SFH data product is listed in Table 5.

Figure 4 shows synthetic images of a simulated galaxy from TNG50 (subhalo ID=107965) at $z = 1.53$ across multiple observatories, including HST, JWST, Ru-

Table 3. Synthetic Datacube FITS File Extensions

FITS Extension Name	Data Type	Description
<i>Imaging Data (2D Broadband Images)</i>		
NODUST_[FILTER]	2D Image	Photometric flux map for a given filter without dust attenuation.
DUST_[FILTER]	2D Image	Photometric flux map for a given filter with dust attenuation.
<i>IFU Data (3D Spectral Cubes)</i>		
OBS_SPEC_NODUST	3D Cube	Observed-frame spectra (λ , y , x) for each pixel without dust.
OBS_SPEC_DUST	3D Cube	Observed-frame spectra (λ , y , x) for each pixel with dust.
<i>Ancillary Data</i>		
WAVELENGTH_GRID	Binary Table	1D array of observed-frame wavelengths for the spectral cubes.

Table 4. Physical Property Maps FITS File Extensions

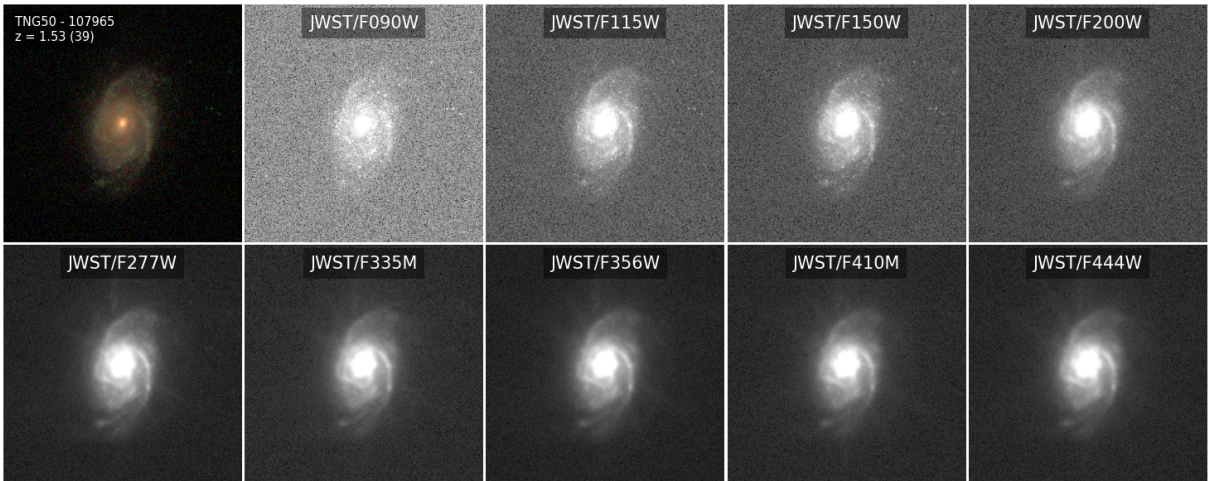
FITS Extension Name	Property Description	Units
<i>Stellar Properties</i>		
STARS_MASS	Stellar mass	M_{\odot}
MW_AGE	Mass-weighted stellar age	Gyr
STARS_MW_ZSOL	Mass-weighted stellar metallicity	Z_{\odot}
LW_AGE_DUST	Light-weighted stellar age with dust attenuation	Gyr
LW_AGE_NODUST	Light-weighted stellar age without dust attenuation	Gyr
LW_ZSOL_DUST	Light-weighted stellar metallicity with dust attenuation	Z_{\odot}
LW_ZSOL_NODUST	Light-weighted stellar metallicity without dust attenuation	Z_{\odot}
SFR_10MYR	SFR averaged over the past 10 Myr	$M_{\odot} \text{ yr}^{-1}$
SFR_30MYR	SFR averaged over the past 30 Myr	$M_{\odot} \text{ yr}^{-1}$
SFR_100MYR	SFR averaged over the past 100 Myr	$M_{\odot} \text{ yr}^{-1}$
<i>Gas, Dust, & Kinematic Properties</i>		
GAS_MASS	Gas mass	M_{\odot}
SFR_INST	Instantaneous SFR derived from gas particle	$M_{\odot} \text{ yr}^{-1}$
GAS_MW_ZSOL	Mass-weighted gas metallicity	Z_{\odot}
DUST_MEAN_AV	Mean dust attenuation (A_V) among star particles	mag
STARS_MW_VEL_LOS	Mass-weighted LOS stellar velocity	km s^{-1}
GAS_MW_VEL_LOS	Mass-weighted LOS gas velocity	km s^{-1}
STARS_VEL_DISP_LOS	LOS stellar velocity dispersion	km s^{-1}
GAS_VEL_DISP_LOS	LOS gas velocity dispersion	km s^{-1}
LW_VEL_LOS_DUST	LOS light-weighted stellar velocity with dust attenuation	km s^{-1}
LW_VEL_LOS_NODUST	LOS light-weighted stellar velocity without dust attenuation	km s^{-1}
LW_VEL_LOS_NEBULAR	LOS Light-weighted nebular velocity	km s^{-1}
GAS_LOGU	Ionization parameter in logarithmic scale	Dimensionless

bin/LSST, and the Roman Space Telescope. For this, we used SSP grids generated with FSPS and applied the “line-of-sight” dust method and the SKIRT-like dust attenuation curve with adaptive slope, bump amplitude, and bump width, as described in Section 2.2.5. The top-left panel displays a color composite image generated from JWST filters F115W (blue), F150W (green), and F200W (red) using the `make_lupton_rgb` function (R. Lupton et al. 2004) from the `astropy` package. These images have a spatial sampling of $0.03 \text{ arcsec pixel}^{-1}$ and do not contain simulated noise (to be described in

the next section). The physical property maps of this galaxy are shown in Figure 5, while Figure 7 shows the galaxy’s resolved SFH. In the latter, the top-left panel shows the map of the spatially resolved lookback time for 50% mass assembly (`T_50_PERCENT`). The remaining panels illustrate the SFH (top right), metallicity history (bottom left), and stellar mass growth (bottom right), comparing the central region ($r < 3 \text{ kpc}$) with the disk ($3 < r < 15 \text{ kpc}$).

Table 5. Spatially Resolved Star Formation History Data Products

Property Description	FITS Extension Name	Description	Unit
<i>3D Data Cubes (y, x, lookback time)</i>			
Star Formation Rate	SFR	Average SFR in each time bin	$M_{\odot} \text{ yr}^{-1}$
Initial Stellar Mass Formed	MASS	Sum of initial stellar masses in bin	M_{\odot}
Cumulative Stellar Mass	CUMUL.MASS	Total stellar mass formed up to that time	M_{\odot}
Mass-Weighted Metallicity	METALLICITY	Mass-weighted average metallicity	Z_{\odot}
Number of Stars	N_STARS	Number of star particles in bin	count
<i>2D Data Maps</i>			
Mass Assembly Times	T_5_PERCENT	Lookback time for 5% mass assembly	Gyr
	T_10_PERCENT	Lookback time for 10% mass assembly	Gyr
	T_25_PERCENT	Lookback time for 25% mass assembly	Gyr
	T_50_PERCENT	Lookback time for 50% mass assembly	Gyr
	T_75_PERCENT	Lookback time for 75% mass assembly	Gyr
	T_95_PERCENT	Lookback time for 95% mass assembly	Gyr
<i>1D Data Array</i>			
Lookback Time Bins	LOOKBACK_TIME.BINS	Midpoints of the lookback time bins	Gyr

**Figure 8.** Example of the post-processed images of the TNG50-107965 galaxy. The images are processed assuming the JADES (D. J. Eisenstein et al. 2026) deep imaging observational characteristics and PSFs. More details about the observational parameters will be given in Section 4.1.

3.2. Adding Observational Effects

To generate realistic synthetic data cubes, `GalSyn` is equipped with functionalities to add observational effects that include point spread function (PSF) convolution, noise simulation, and spatial resampling to a desired pixel scale. This can be performed using `observe` module. In the future update of the code, we plan to incorporate other public packages (e.g., `Galsim`, B. T. P. Rowe et al. 2015; `romanisim`; `MIRAGE`) for more realistic simulation of observational effects.

The first step is to resample the synthetic images to a user-defined pixel scale, which can be set independently

for each filter. This resampling process is done following procedures described in Section 2.5.

The next step is PSF convolution. A PSF is the characteristic blurred shape a telescope and camera system records when observing a point source of light, like a distant star. This PSF determines the image’s fundamental resolution. In `GalSyn` processing, the PSF must be provided by the user as a 2D FITS image file. Each filter requires its own corresponding PSF file. This allows for wavelength-dependent variations in the blurring effect.

In terms of noise simulation, `GalSyn` simulates the two primary sources of observational noise: photon shot noise from the astronomical source and background

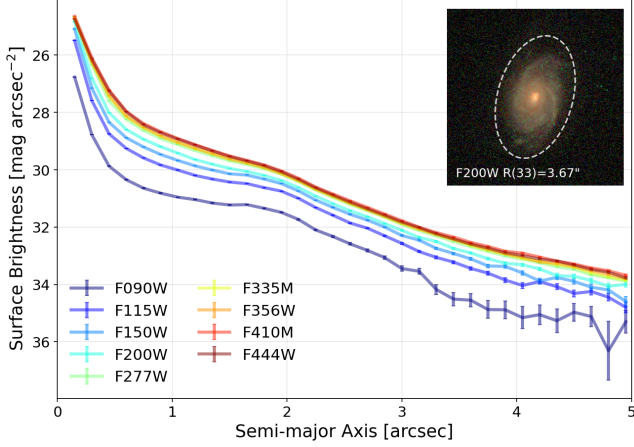


Figure 9. Multi-wavelength surface brightness radial profiles of the TNG50-107965 galaxy. The profiles show a characteristic two-component structure: a steep central gradient ($R < 1$ arcsec) and a shallower exponential disk. The galaxy signal traced to extreme depths of ~ 34 – 36 mag arcsec $^{-2}$. The white dashed line in the inset RGB map indicates the isophotal line of 33 mag arcsec $^{-2}$ in F200W.

noise from the sky and instrument electronics. It achieves this by mimicking known (i.e., empirical) or expected noise characteristics rather than predicting them from detailed instrument parameters. This approach simplifies the process, as users can input desired noise levels, whether determined empirically or from an Exposure Time Calculator (ETC), without needing complex or often unavailable instrument data. This method provides the flexibility to simulate noise for any instrument.

For the synthetic imaging, noise is calculated for each filter based on user-defined observational magnitude limits at given S/N thresholds. The process converts the ideal, noise-free image into a realistic mock observation. The ideal flux of each pixel is first converted into f_λ units of erg s $^{-1}$ cm $^{-2}$ Å $^{-1}$ if it is not the original unit, and then converted into the expected number of photon counts that the detector would register. First, the flux per pixel is converted to an AB magnitude:

$$m_{\text{AB}} = -2.5 \cdot \log_{10}(f_\nu) - 48.6 \quad (19)$$

where $f_\nu = f_\lambda \cdot \frac{\lambda_p^2}{c}$ is the flux density in erg s $^{-1}$ cm $^{-2}$ Hz $^{-1}$. Then, the expected source counts are calculated using the instrumental zero-point magnitude (m_{zp}) and the exposure time (t_{exp}):

$$C_{\text{src}} = t_{\text{exp}} 10^{0.4(m_{\text{zp}} - m_{\text{AB}})}. \quad (20)$$

The background noise is derived from the specified limiting magnitude (m_{lim}) and the signal-to-noise ratio (SNR_{lim}) achieved at that limit within a given aperture.

First, the total counts from a source at the limiting magnitude (C_{lim}) are calculated as:

$$C_{\text{lim}} = t_{\text{exp}} \cdot 10^{0.4(m_{\text{zp}} - m_{\text{lim}})} \quad (21)$$

The SNR is defined as $\text{SNR} = \frac{C_{\text{src}}}{\sqrt{C_{\text{src}} + C_{\text{bg}}}}$, where C_{bg} is counts associated with the background. Rearranging to solve for the variance of the background counts ($\sigma_{\text{bg, apert}}^2 = C_{\text{bg}}$) within the aperture gives:

$$\sigma_{\text{bg, apert}}^2 = \left(\frac{C_{\text{lim}}}{\text{SNR}_{\text{lim}}} \right)^2 - C_{\text{lim}} \quad (22)$$

The standard deviation of the background counts in the aperture is $\sigma_{\text{bg, apert}}$. This is then converted to a per-pixel standard deviation by dividing by the square root of the aperture area in pixels ($A_{\text{apert, pix}}$):

$$\sigma_{\text{bg, pix}} = \frac{\sigma_{\text{bg, apert}}}{\sqrt{A_{\text{apert, pix}}}} \quad (23)$$

The final noisy image is created by combining the simulated noise components. The source noise is simulated by drawing from a Poisson distribution with the expected source counts as the mean:

$$N_{\text{src}} \sim \text{Poisson}(\lambda = C_{\text{src}}), \quad (24)$$

whereas the background noise is simulated by drawing from a Gaussian (i.e., normal) distribution:

$$N_{\text{bg}} \sim \mathcal{N}(\mu = 0, \sigma = \sigma_{\text{bg, pix}}). \quad (25)$$

The final noisy image, in counts, is then the sum of these two components:

$$C_{\text{noisy}} = N_{\text{src}} + N_{\text{bg}}. \quad (26)$$

This count value is then converted back into physical flux units. The corresponding error (i.e., Root Mean Square, RMS) map is calculated by adding the variances in quadrature, where the variance of the source's shot noise is equal to the expected source counts:

$$\sigma_{\text{total, pix}} = \sqrt{\sigma_{\text{src}}^2 + \sigma_{\text{bg, pix}}^2} = \sqrt{C_{\text{src}} + \sigma_{\text{bg, pix}}^2} \quad (27)$$

This RMS value in counts is also converted back to flux units to provide the final error map.

To illustrate the robustness of this analysis, we show in Figure 8 an example of the post-processing result for the TNG50-107965 galaxy. The images are processed assuming the JADES (D. J. Eisenstein et al. 2026) deep imaging observational characteristics and PSFs, specifically for the subregion jw011800-deep from the DR 5. More details about the observational parameters will be

given in Section 4.1. The F090W image, which has a limiting magnitude of 29.87 (at $S/N=5$ measured on 0.15 arcsec aperture), looks shallower than the other images, which reach deeper limiting magnitudes (> 30).

Figure 9 shows the surface brightness radial profiles across the filters. These profiles demonstrate a characteristic two-component structure across the wavelength. A steep central gradient ($R < 1$ arcsec) transitions into a shallower exponential disk, with the galaxy signal traced to extreme depths of $\sim 34\text{--}36$ mag arcsec $^{-2}$. A consistent vertical offset is observed across the spectrum, where the long-wavelength bands (e.g., F444W) exhibit significantly higher SB than the shorter wavelength bands (e.g., F090W), indicating a globally red stellar population in the galaxy. The increasing error bars and surface-brightness fluctuations beyond $R \approx 4''$ in the F090W band mark the transition into the background-dominated regime. The white dashed line in the inset RGB image indicates the isophotal line of 33 mag arcsec $^{-2}$ in F200W.

3.3. Post-processing of IFU Data Cube

The post-processing of synthetic IFU data cubes in `GalSyn` begins with several spectral and spatial modifications to simulate realistic observational effects. First, the high-resolution synthetic cube is spectrally interpolated onto a user-defined wavelength grid, `desired_wave_grid`. The next step is to spatially resample the cube to a desired output pixel scale, which is performed using the same method as that for the synthetic images. Then, to simulate the effect of a finite instrumental resolution, the spectrum of each spaxel is convolved along the wavelength axis with a 1D Gaussian kernel. The width of this kernel is determined by a user-provided target spectral resolution, $R \equiv \lambda/\Delta\lambda$. The cube is then spatially convolved using a user-defined 3D PSF cube, a FITS file whose wavelength grid must exactly match the `desired_wave_grid`. The convolution is performed slice-by-slice, using the corresponding 2D PSF slice for each wavelength channel to model the wavelength-dependent blurring.

Following these spectral and spatial convolutions, observational noise is injected, also on a slice-by-slice basis. The process follows the same principles as those for the synthetic imaging data cube, but is performed independently for each wavelength slice of the data cube. The key difference is that the input parameters can be functions of wavelength: $m_{zp}(\lambda)$, $t_{exp}(\lambda)$, $m_{lim}(\lambda)$, and $SNR_{lim}(\lambda)$.

The same set of equations outlined in Section 3.2 is used, but they are applied slice-by-slice, iterating through the wavelength axis of the cube. This ensures

that the final 3D data cube and its corresponding 3D RMS error cube have a realistic, wavelength-dependent noise profile.

Figure 10 presents a synthetic IFU datacube of galaxy TNG50-18832 at $z = 3.28$, post-processed to emulate JWST/NIRSpec IFU observations across four configurations: G140M/F100LP, G235M/F170LP, G395M/F290LP, and Prism/CLEAR. To determine the sensitivity limits, we performed systematic signal-to-noise (S/N) simulations using the `Pandemia` exposure time calculator (ETC) engine (K. M. Pontoppidan et al. 2016). We modeled a flat input spectrum in AB magnitudes across a grid of exposure times (10, 20, and 40 ks) and source magnitudes (18–28). For each configuration, the S/N was calculated per pixel on the native detector grid. We derived $5\text{-}\sigma$ sensitivity limits by interpolating the magnitude- S/N relationship at each wavelength point, subsequently passing these limits to the `galsyn` module for noise simulation. A more detailed description of the procedure for estimating the sensitivity limits is given in Appendix C.

The spectra shown in Figure 10 correspond to a 40 ks exposure time (20 ks for Prism/CLEAR). For the PSF convolution, we modeled NIRSpec/IFU PSFs using `STPSF` (M. D. Perrin et al. 2014). In the figure, the red curve denotes the intrinsic spectrum without observational effects. The panels in the top row show [OIII] λ 5007 flux map, H α flux map, and a color composite image. The white box in each panel shows the NIRSpec IFU field of view.

To illustrate the robustness of the noise simulation in `GalSyn`, we compare the S/N profiles of the spectra across multiple instrument configurations with those derived using the `Pandemia` ETC engine. The comparison is shown in Figure 11. The red profiles are the S/N derived using the ETC, while the other profiles are the S/N recovered by `GalSyn`.

4. FIRST DATA RELEASE

In this introductory paper, we present the first public data release of `GalSyn` to demonstrate its core capabilities. This release includes three distinct data cube categories generated from the IllustrisTNG simulation suites: four mock extragalactic survey fields, the progenitors of local massive galaxies ($\log(M_{*,z=0}/M_{\odot}) > 10.5$), and a sample of major-merging systems. For each galaxy, the data products consist of synthetic imaging across 47 filters (spanning JWST, HST, Euclid, Rubin/LSST, and the Roman Space Telescope), a comprehensive suite of physical property maps (see Section 2.3), and spatially resolved SFHs.

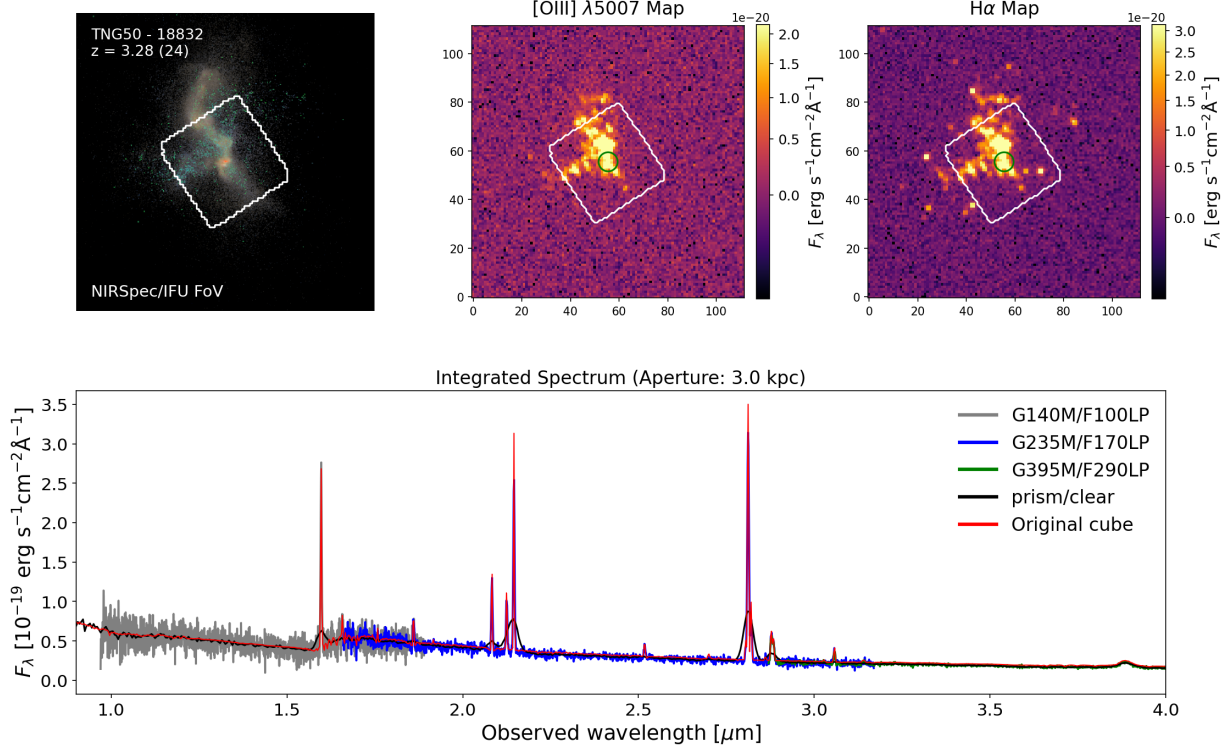


Figure 10. Post-processed synthetic IFU datacube of galaxy TNG50-18832 at $z = 3.28$, emulating JWST/NIRSpec IFU observations across four configurations: G140M/F100LP, G235M/F170LP, G395M/F290LP, and Prism/CLEAR. The noise is simulated based on the estimated 5σ limiting magnitudes of the instruments derived from the *Pandemia* ETC engine (K. M. Pontoppidan et al. 2016). The exposure time is set to 20 ks for Prism/CLEAR and 40 ks for the other instruments. The red curve in the bottom panel denotes the intrinsic spectrum without observational effects. The panels in the top row show, from the left to right: a color composite image, [OIII] λ 5007 flux map, and H α flux map. The white box in each panel shows the NIRSpec IFU field of view.

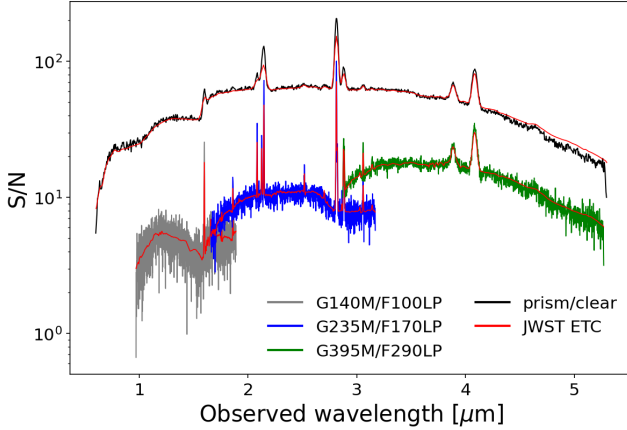


Figure 11. S/N profiles of spectra across multiple instrument configurations, as shown in Figure 10, derived from *GalSyn* simulations and estimated using the *Pandemia* ETC engine (shown in red). The two methods show very good agreement, demonstrating the good recovery of observational parameters by *GalSyn*.

We implement the “line-of-sight” dust method with three different dust attenuation curves: (1) dust0-

S18K13: the option 0 dust model with an adaptive slope following the δ - A_V relation from S. Salim et al. (2018) and bump amplitude following the B - δ relation from M. Kriek & C. Conroy (2013); (2) dust0-skirt-like: the option 0 dust model with an adaptive slope, bump amplitude, and bump width following the δ - B - γ - A_V correlations inferred from the NIHAO-SKIRT synthetic spectroscopic cubes (N. Faucher et al. 2023); and (3) the option 6 dust model: Milky Way dust extinction law from E. L. Fitzpatrick (1999).

To capture a representative range of viewing geometries, we produce these data cubes at four distinct viewing angles: A1 ($\theta = 45^\circ$, $\phi = 45^\circ$), A2 ($\theta = 0^\circ$, $\phi = 0^\circ$), A3 ($\theta = 90^\circ$, $\phi = 90^\circ$), and A4 ($\theta = 90^\circ$, $\phi = 0^\circ$). These datasets are publicly available at https://github.com/aabdurrouf/GalSyn_dr1.

4.1. Mock Extragalactic Survey Fields

The current rapid expansion of galaxy redshift surveys necessitates high-fidelity simulations to aid in observational design, pipeline testing, and the interpretation of complex datasets. Here, we produce four mock survey

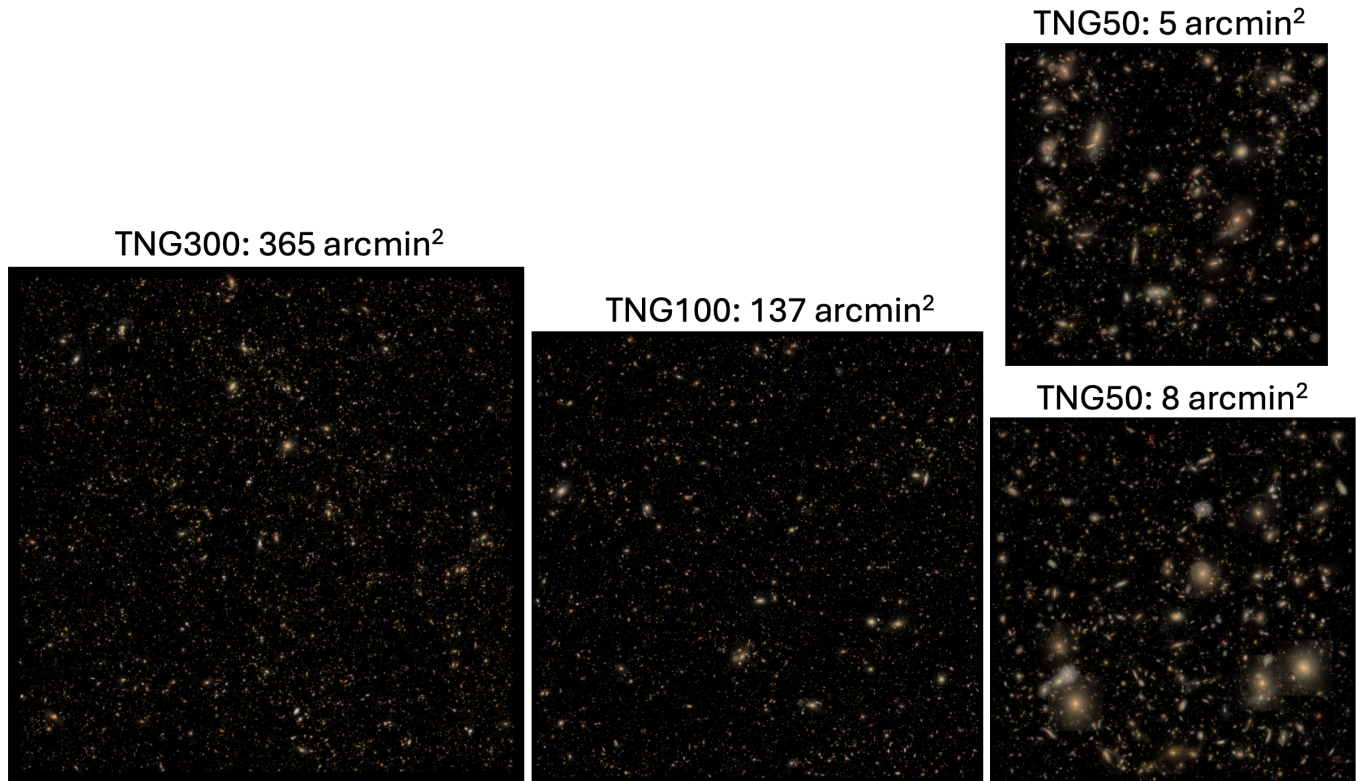


Figure 12. Mock extragalactic survey fields generated from the three IllustrisTNG simulation suites (TNG50-1, TNG100-1, and TNG300-1) using the lightcone catalogs from [G. F. Snyder et al. \(2023\)](#). These fields cover areas of 5, 8, 137, and 365 arcmin². These idealized mosaics implement the LOS dust method with the dust0-skirt-like prescription at viewing angle A1, excluding observational noise or PSF effects. The color composite images are created using JWST images: F115W (blue), F150W (green), and F200W (red).

fields using the lightcone catalogs from [G. F. Snyder et al. \(2023\)](#):

- 5 arcmin² (TNG50) and 8 arcmin² fields generated from TNG50-1
- 137 arcmin² field generated from TNG100-1
- 365 arcmin² field generated from TNG300-1

These mosaics utilize the snapshots, subhalo IDs, and celestial coordinates (RA and DEC) assigned by the [G. F. Snyder et al. \(2023\)](#) lightcone catalogs. For every galaxy in these catalogs, we generate a synthetic imaging data cube using `GalSyn`. The image size is set to encompass at least 99% of the total stellar mass of the subhalo associated with the galaxy. Mosaics are constructed by creating a blank FITS array using the `Astropy` package ([Astropy Collaboration et al. 2013, 2018](#)), defining a World Coordinate System (WCS) centered at (RA, DEC) = (0, 0), and populating the field with the individual galaxy synthetic images.

In addition to the mosaics, we provide isolated data cubes for each constituent galaxy. These cutouts represent the isolated subhalos, free from the crowded mo-

saic environment. Each cube contains 47-filter imaging, physical property maps, and spatially resolved SFHs. We also include catalogs of integrated physical properties, including stellar, gas, dark matter, and black hole masses, as well as SFRs, half-stellar-mass radii, and metallicities. Figure 13 shows a examples of 24 galaxies from the TNG50-11-10 field, covering a redshift range of $0.2 < z < 4.5$ and stellar masses $M_* > 10^{9.5} M_\odot$.

These individual cubes enable diverse scientific analyses, such as systematic comparisons with observations to gain physical insights. While a full assessment of `GalSyn`'s physical modeling is deferred to a forthcoming paper, we present a preliminary evaluation using color-color diagnostics. Specifically, we employ observed-frame JWST filter combinations that mimic the rest-frame UVJ diagram (e.g., [R. J. Williams et al. 2009](#)). This diagnostic is widely used to identify quiescent galaxies due to its effectiveness in breaking the degeneracy between stellar aging and dust attenuation. To approximate the rest-frame $U - V$ color, we select filter pairs that bracket the rest-frame 4000 Å break.

We select galaxies with $M_* > 10^7 M_\odot$ from the TNG50-11-10 and TNG50-12-11 fields (viewing an-



Figure 13. Representative image stamps of 24 galaxies selected from the TNG50-11-10 field. Extracted from TNG subhalo cutouts, these data cubes provide an isolated view of each system. In this example, galaxies are seen from the A1 viewing angle ($\theta = 45^\circ$, $\phi = 45^\circ$). The physical scale of each stamp is indicated in the bottom-right corner of the respective panels. The color composite images are created using JWST filters: $z < 0.2$ (F115W, F150W, F200W), $0.2 < z < 1.2$ (F150W, F200W, F277W), and > 1.2 (F200W, F277W, F356W).

gle A1) and group them in four redshift bins ($z \approx 0.5, 1.5, 2.5, 3.5$) with a width of $\Delta z = \pm 0.4$. We then calculate photometry of each galaxy within a circular aperture of twice the half-stellar mass radius. Figure 14 shows the resulting color-color distributions: the top row displays results without dust attenuation, while the middle and bottom rows show the results that implement the dust0-skirt and dust0-S18K13 models, respectively. The color coding represents median sSFR of galaxies in the bins. At $z \approx 0.5$ and 1.5, models including dust attenuation show a clear separation for quiescent galaxies (sSFR $\lesssim 10^{-10.5} \text{ yr}^{-1}$), consistent with the R. J. Williams et al. (2009) selection box. In contrast, dust-free models result in a more scattered vertical distribution, with many quiescent galaxies falling below the selection region. From the color-color distribution, we see a good consistency between the results obtained with the dust0-skirt-like and dust0-S18K13.

Finally, we provide versions of these mosaics that include realistic observational effects (Section 3.2). These are designed to emulate JADES deep imaging (D. J. Eisenstein et al. 2026), specifically the jw011800-deep subregion. We adopted empirical photometric characteristics of this field, including PSF images, limiting magnitudes ($S/N = 5$ at $0.15''$), and an exposure time of 87 hours (B. D. Johnson et al. 2026).

An example of a post-processed mosaic for TNG50-11-10 is shown in the left panel of Figure 15. The right panel shows the correlation between the S/N and on-source magnitudes measured within a $0.15''$ radius aperture. The star symbols denote the empirical limiting magnitudes used as input parameters for GalSyn; as shown, these values are perfectly recovered in the simulated data. Further details regarding the JADES deep imaging characteristics and the fidelity with which GalSyn reproduces them are provided in Appendix B.

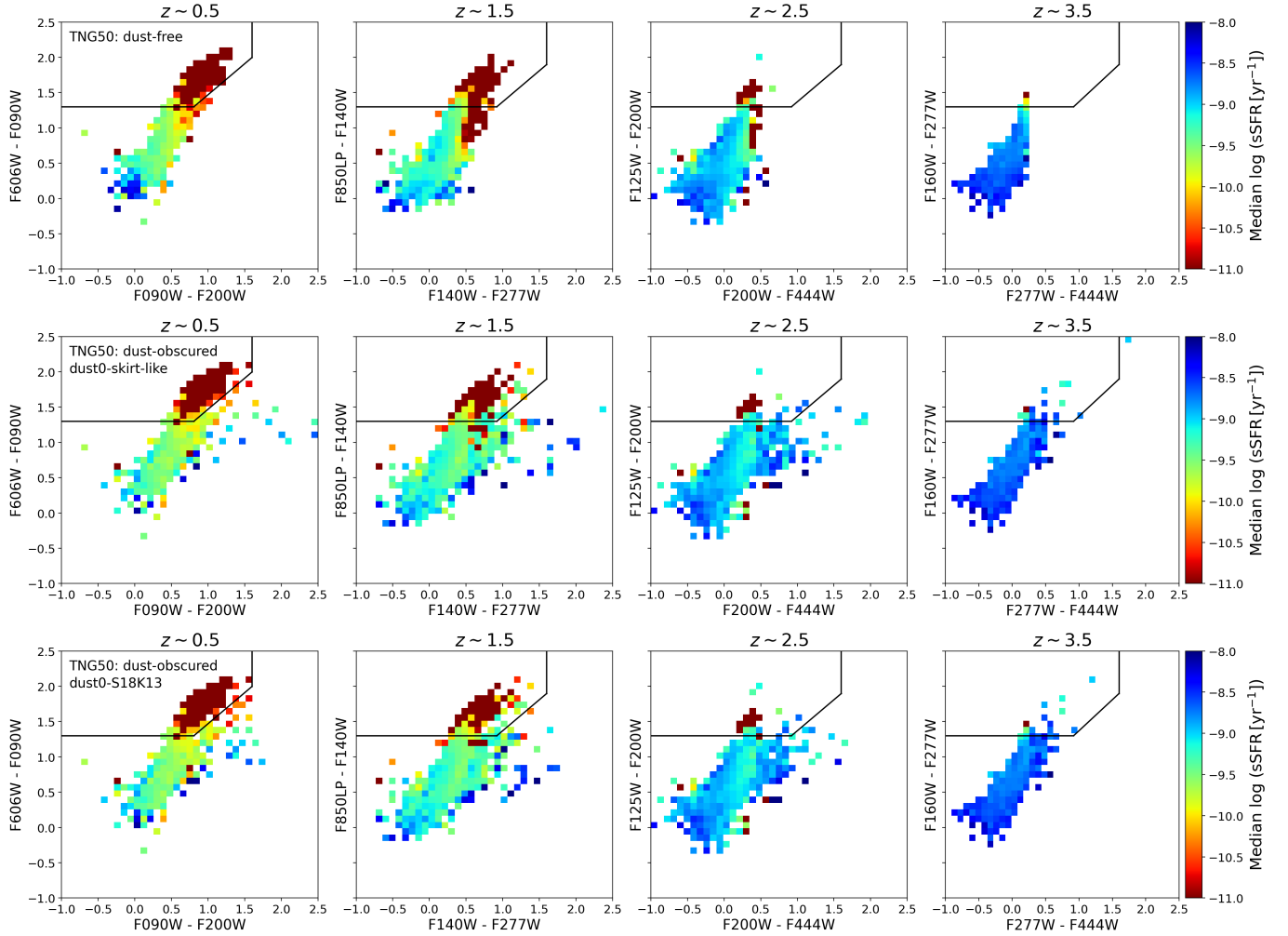


Figure 14. JWST color-color diagrams across four redshift bins, designed to mimic the rest-frame UVJ diagram. The top, middle, and bottom rows show results for no dust, dust0-skirt-like, and dust0-S18K13 models, respectively. Bins are color-coded by median sSFR of their constituent galaxies. The black line indicates the quiescent selection box from R. J. Williams et al. (2009). The inclusion of dust (middle and bottom) significantly improves the alignment of quiescent galaxies with empirical selection boundaries.

Given the wide range of potential observational depths, we do not include observational effects in the individual galaxy data cubes. Instead, we provide these effects only for the mosaics, specifically tailored to the characteristics of the JADES deep subregion. However, users can easily extend this analysis to other observational configurations by using function `GalsynMockObservation_mosaic` in `observe` module.

4.2. Progenitors of Massive Galaxies

The recent discovery of massive, mature (quiescent) galaxies at high redshifts ($z > 3$) by JWST has challenged existing galaxy formation models, raising fundamental questions about how such systems assembled substantial stellar mass so early in cosmic time (e.g., A. C. Carnall et al. 2023; N. S. Haryana et al. 2025; W. M. Baker et al. 2025). To facilitate a systematic

exploration of these “early bloomers” and their evolutionary pathways, we provide synthetic data cubes for the progenitors of 290 massive galaxies identified in the TNG50 $z = 0$ snapshot with stellar masses $\log(M_{*,z=0}/M_{\odot}) > 10.5$. By focusing on the $z = 0$ descendants, this sample allows users to perform “galaxy archaeology” in reverse, tracing the structural and photometric properties of today’s most massive systems back to their infancy in the early universe.

The progenitor histories are tracked using the `SubLink` algorithm (V. Rodriguez-Gomez et al. 2015), which connects subhalos across snapshots by mapping unique particle IDs to determine robust descendant-progenitor relationships. We track these lineages from the local universe out to $z = 5$ at intervals of approximately $\Delta z \approx 0.2$. This fine temporal resolution results in 26 snapshots per lineage and a total sample of 7,540 indi-

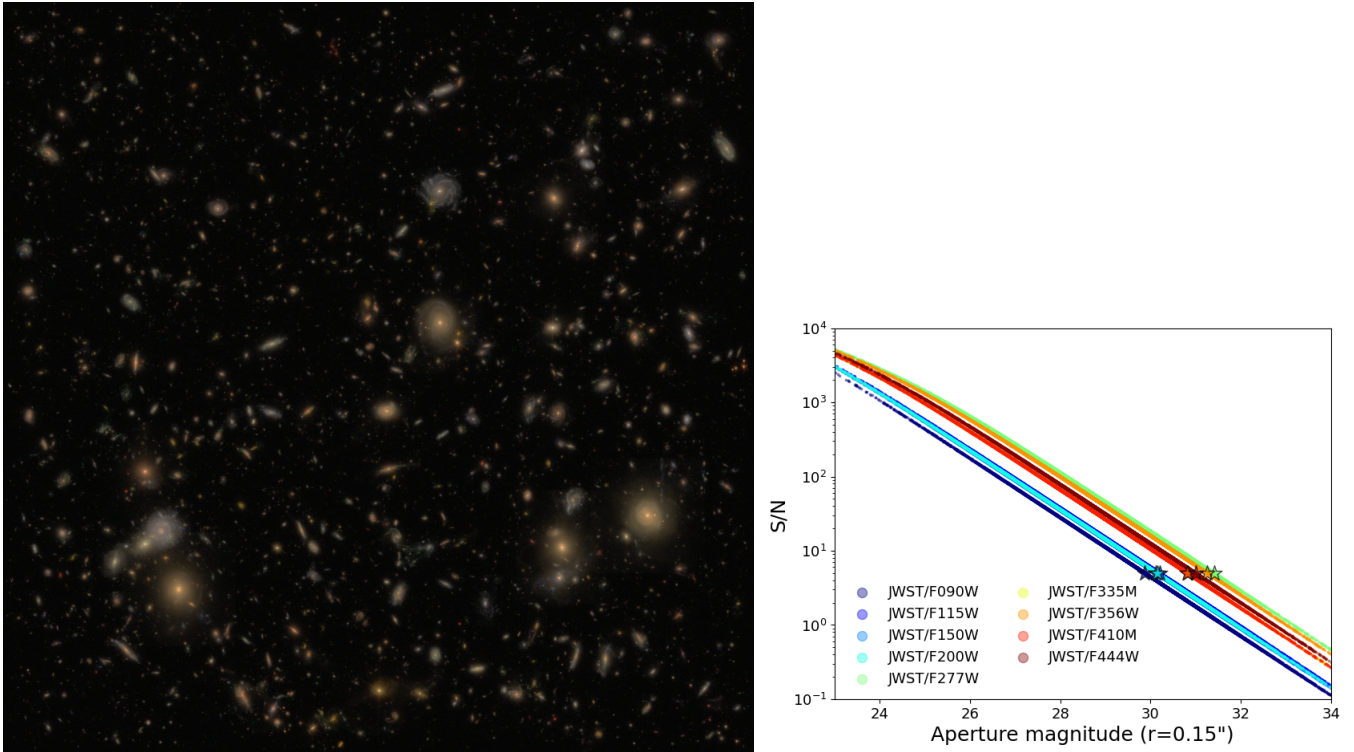


Figure 15. *Left:* Color composite of the TNG50-11-10 field with added observational effects emulating the JADES deep survey (jw011800-deep). *Right:* S/N versus on-source magnitude within a $0.15''$ radius aperture. Star symbols denote the target empirical limiting magnitudes ($S/N = 5$), which are precisely recovered by the GalSyn noise simulation.

vidual galaxies. This systematic time-stepping is crucial for capturing short-lived evolutionary phases, such as rapid starbursts or AGN-driven quenching events, which might be missed in broader redshift samplings.

Figure 16 shows the stellar mass assembly histories (stellar mass vs. redshift) for this sample, with tracks color-coded by the final stellar mass attained at $z = 0$. Overlaid on these tracks are representative postage stamps depicting the morphological evolution of two specific progenitors: one focusing on a lower-mass descendant ($\sim 10^{10} M_{\odot}$) and another reaching a final mass of $\sim 10^{10.5} M_{\odot}$. Qualitatively, the figure reveals a clear divergence in growth modes: the most massive systems tend to assemble a significant fraction of their stellar mass early on ($z \gtrsim 2.5$), followed by a phase of relatively modest accretion or quiescent evolution. In contrast, less massive systems exhibit a more continuous, gradual growth profile. These synthetic observations allow us to quantify exactly when and where these mass-assembly differences become photometrically detectable.

These data cubes serve as a useful laboratory for studying the spatially resolved evolution of massive galaxy progenitors. They enable us to move beyond integrated properties and examine the spatial distribution of star formation, the buildup of stellar disks and bulges, and the specific physical mechanisms, such as

environmental effects or internal feedback, that lead to the cessation of star formation. Ultimately, this dataset provides the community with a self-consistent bridge between the high-redshift “progenitors” seen by JWST and the well-studied massive “descendants” in the local universe, offering a unique resource for testing the physics of galaxy evolution.

4.3. Major-merger Systems

Galaxy mergers are among the most transformative events in the cosmic life cycle, capable of triggering intense starbursts, fueling rapid supermassive black hole growth, and fundamentally reshaping galaxy morphology. To facilitate the study of these violent transitions, we have curated a specialized sample of major merger events ($M_{*,1}/M_{*,2} \geq 1/4$) occurring within the lineages of the massive galaxy progenitors described in Section 4.2. Drawing from the IllustrisTNG merger history catalogs (V. Rodriguez-Gomez et al. 2017; L. Eisert et al. 2023), we identified 259 unique major mergers spanning the redshift range $0 < z < 5$.

Unlike the progenitor sample, which follows a rigid temporal grid, this dataset is event-driven; we extract snapshots that specifically capture the major-merger event, based on the merger catalogs. A key technical distinction in this release is that these synthetic data

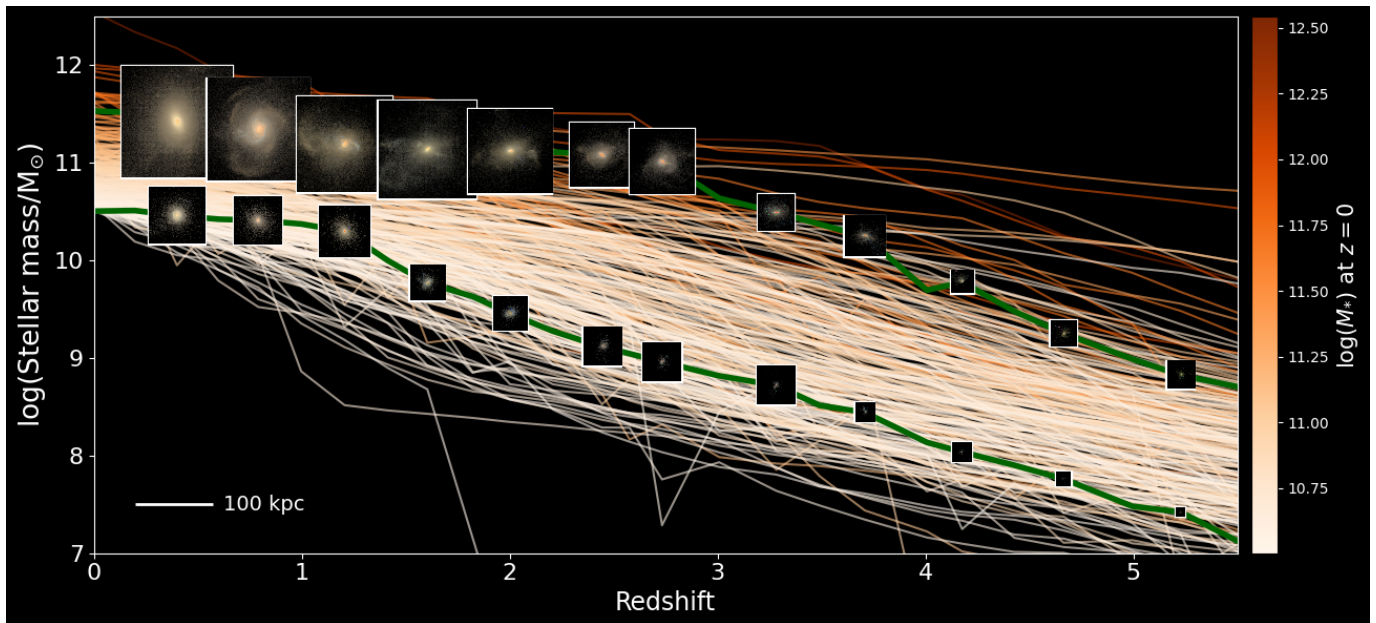


Figure 16. Stellar mass assembly histories for the progenitors of 290 massive galaxies ($\log(M_{*,z=0}/M_{\odot}) > 10.5$) across the redshift range $0 < z < 5$. The tracks are color-coded by their $z = 0$ descendant mass, illustrating the “early-and-fast” growth characteristic of the most massive systems compared to the more gradual assembly of lower-mass galaxies. Representative JWST color-composite stamps are overlaid to show the morphological and photometric evolution along two example tracks.

cubes are generated using parent halo cutouts rather than isolated subhalos. By including all particles associated with the parent Friends-of-Friends (FoF) group, we ensure that both interacting progenitors, as well as any tidal bridges, tails, or diffuse intra-halo light, are preserved in the synthetic observations. This is essential for capturing the complex environments that define merging systems.

Beyond the raw photometry, the data cube includes the physical property maps (see Section 2.3). These sets provide a valuable resource for a variety of scientific analyses, such as developing and training machine learning algorithms for merger identification. Traditional methods often rely on simple morphological asymmetries or non-parametric statistics (e.g., Gini, M_{20}); however, our datasets provide a multi-wavelength training set that includes realistic synthetic images and spatially resolved physical property maps. These can be used for investigating how merger signatures vary across different filters. Furthermore, the spatially resolved SFHs provide mapping exactly where star formation is enhanced, whether it is concentrated in the nuclei due to gas inflows or triggered in the tidal tails.

Finally, the inclusion of multiple viewing angles (A1–A4) for each merger event addresses the significant challenge of projection effects in observational studies. A system that appears as a late-stage merger from one perspective may look like a projected pair from another. By providing these multi-angle synthetic cubes,

this data release enables a statistical assessment of how orientation influences the measured merger rates and the derived physical properties of interacting systems. This dataset thus serves as a comprehensive bridge between theoretical predictions of merger-driven evolution and the diverse morphologies observed in deep extragalactic fields. Currently, the data release focuses exclusively on the major mergers associated with massive galaxy progenitors. Future releases will expand this catalog to include mergers across a broader range of descendant masses, as well as minor merger events.

5. SUMMARY AND OUTLOOKS

In this paper, we introduce **GalSyn** (Galaxy Synthesizer), a modular and flexible Python package for generating synthetic spectrophotometric observations from hydrodynamical galaxy simulations. **GalSyn** bridges the gap between numerical simulations and real observations by implementing an efficient particle-by-particle spectral modeling approach, which enables the rapid production of large synthetic datasets well-suited to population studies and statistical analyses of galaxies across a wide redshift range.

The core capabilities of **GalSyn** can be summarized as follows. The package accepts a simulation-agnostic, standardized HDF5 input format, enabling its application to a wide range of hydrodynamical simulations. It provides users with unprecedented control over the spectral synthesis process, including the choice of SPS engine

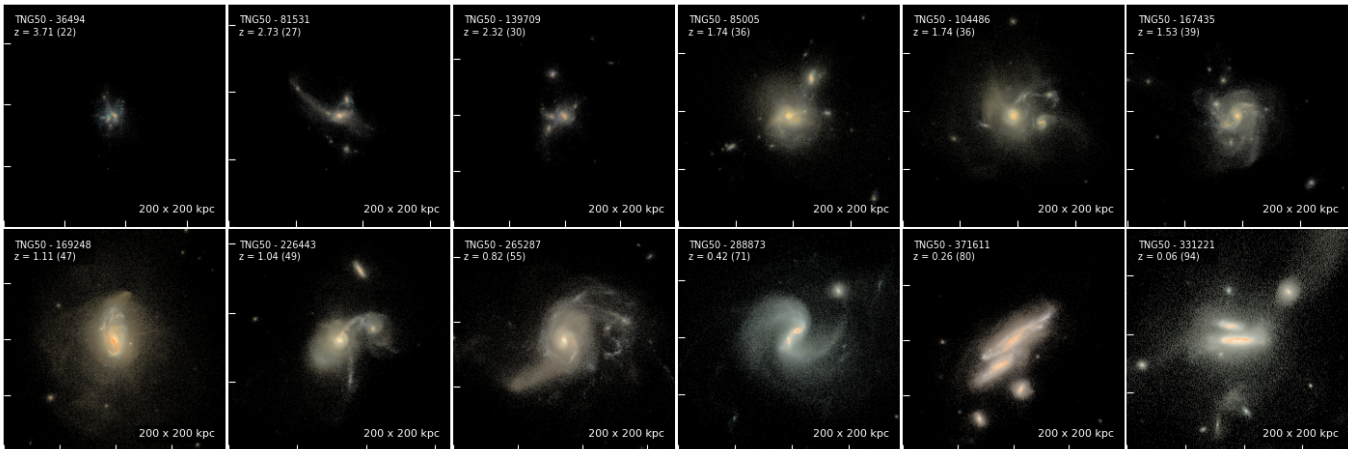


Figure 17. A collage of color-composite stamps showcasing examples of major-merging systems in the first data release. Unlike isolated subhalo cutouts, these images are generated from parent halo data to capture the full spatial extent of tidal features, bridges, and multiple interacting nuclei. The color composite images are created using the same JWST filter combinations as those used for Figure 13.

(FSPS or `bagpipes`), stellar isochrone sets, spectral libraries, and initial mass functions. A spatially varying ionization parameter is computed self-consistently from the local gas properties of each pixel and is used to model the nebular emission from young stellar populations. `GalSyn` implements a decoupled kinematics model that independently Doppler-shifts the stellar continuum and nebular emission components, reproducing the observational signatures of distinct gas and stellar kinematic fields that are critical for realistic synthetic IFU data. Dust attenuation is modeled at the spatially resolved level through either a line-of-sight gas column density method or an SFR-surface-density-based approach. A comprehensive suite of dust attenuation laws is provided, including both fixed and adaptive prescriptions that allow the shape of the attenuation curve to vary with the local A_V . `GalSyn` also provides post-processing features to add observational realism, including PSF convolution, noise simulation, and spatial resampling. Beyond synthetic imaging and IFU data cubes, `GalSyn` reconstructs spatially resolved physical property maps and star formation histories, enabling direct spatially resolved comparison with observational data.

Together with this paper, we present the first public data release of synthetic galaxy observations generated from the IllustrisTNG simulation suites. This release comprises four mock extragalactic survey fields covering areas of 5, 8, 137, and 365 arcmin² drawn from TNG50-1, TNG100-1, and TNG300-1, respectively, synthetic data cubes for the progenitors of 290 local massive galaxies ($\log(M_{*,z=0}/M_\odot) > 10.5$) tracked from $z = 0$ to 5, and 259 major-merger systems identified within those progenitor lineages. For each galaxy, the data products include synthetic imaging in 47 filters span-

ning HST, JWST, Euclid, Rubin/LSST, and the Roman Space Telescope, a comprehensive suite of spatially resolved physical property maps, and spatially resolved star formation histories. Datasets are provided at four distinct viewing angles and under three dust attenuation prescriptions.

Looking ahead, several extensions to `GalSyn` are planned for future work. First, modules for natively handling simulation data from EAGLE and other hydrodynamical simulations (such as COLIBRE, [J. Schaye et al. 2025](#)) will be added. Second, the current `GalSyn` framework models dust attenuation but defers dust emission; the incorporation of far-infrared and submillimeter emission from heated dust grains is a natural next step, which will extend the utility of `GalSyn` to long-wavelength observatories such as ALMA and *Herschel*. Third, a forthcoming companion paper will present a systematic investigation of how different choices of dust attenuation law impact the observable photometric and spectroscopic properties of simulated galaxies, directly exploiting the flexibility of `GalSyn`'s modular design. Fourth, the first data release presented here focuses on IllustrisTNG; future releases will incorporate galaxies from complementary simulation suites to enable broader cross-simulation comparisons and to expand the available training sets for machine learning applications. All data products from the first release are publicly available at https://github.com/aabdurrouf/GalSyn_dr1.

Finally, a particularly promising avenue for future development is the integration of `GalSyn` into parameter estimation and statistical inference frameworks. The computational efficiency of `GalSyn` makes it well-suited as a forward model within simulation-based inference

(SBI) frameworks (also known as likelihood-free inference). In this framework, `GalSyn` would serve as the simulator, generating large ensembles of synthetic observations across a broad range of physical parameter combinations. It is possible to further accelerate the synthesis process in `GalSyn` by re-implementing key components of `GalSyn` using JAX.

ACKNOWLEDGMENTS

The authors acknowledge the Indiana University Perseus Technology Institute (PTI) and UITS for providing supercomputing and visualization resources on Big Red 200 and Quartz that have contributed to the research results reported within this paper. The computations reported in this paper were (in part) performed using resources made available by the Flatiron Institute. The Flatiron Institute is a division of the Simons Foundation.

The IllustrisTNG simulations were undertaken with compute time awarded by the Gauss Centre for Supercomputing (GCS) under GCS Large-Scale Projects GCS-ILLU and GCS-DWAR on the GCS share of the supercomputer Hazel Hen at the High Performance Computing Center Stuttgart (HLRS), as well as on the machines of the Max Planck Computing and Data Facility (MPCDF) in Garching, Germany.

AUTHOR CONTRIBUTIONS

All authors contributed to the work that resulted in this paper.

Software: FSPS (C. Conroy et al. 2009; C. Conroy & J. E. Gunn 2010), Python FSPS (B. Johnson et al. 2024), Bagpipes (A. C. Carnall et al. 2018), piXedfit (Abdurro’uf et al. 2021, 2022)

APPENDIX

A. ROBUSTNESS OF SSP INTERPOLATION METHODS

The core of `GalSyn`’s efficiency lies in its ability to map physical properties from simulation particles to synthetic spectra using pre-computed SSP and nebular emission grids. As described in Sections 2.1.2 and 2.2.3, these grids are discretized across age, metallicity, and ionization parameter. However, because simulation particles possess a continuous range of physical properties, the accuracy of the resulting synthetic spectra depends on the interpolation scheme used to traverse these grids.

Here, we quantify the trade-offs between various interpolation methods and grid densities to provide users with a baseline for model reliability. To assess the robustness of our spectral synthesis, we experiment by comparing interpolated spectra against “ground truth” models (spectra generated directly by the SPS engine without interpolation). We tested three interpolation methods: nearest neighbor, linear, and cubic spline. These methods are applied across eight SSP grid configurations of increasing density, labeled by the number of bins in Age (A), Metallicity (Z), and Ionization (U): A50_Z50_U5, A50_Z50_U10, A100_Z100_U5, A100_Z100_U10, A200_Z200_U5, A200_Z200_U10, A300_Z300_U5, and A300_Z300_U10. The accuracy was measured via the percentage residual, defined as $100 \times (F_{\text{interp}} - F_{\text{truth}}) / F_{\text{truth}}$, across the full wavelength range.

The results of this comparison are summarized in Figure 18. The nearest neighbor method consistently shows the highest residuals ($\gtrsim 3\%$) across the whole wavelength range. Conversely, the linear and cubic methods significantly reduce these errors. For the lower-density A50_Z50 grids, even higher-order interpolation struggles to capture sharp spectral features (e.g., the 4000Å break or emission lines) accurately. However, once the grid density reaches A100_Z100 or higher, the residuals drop below $\sim 1 - 2\%$ for both linear and cubic methods. Increasing the U resolution from 5 to 10 bins (bottom panels vs. top panels) provides a marginal but noticeable improvement in the recovery of nebular-dominated spectra.

While the cubic method provides the most robust recovery with minimal residuals, it is the most computationally expensive, significantly increasing the processing time per galaxy. The nearest neighbor method, while fast, is insufficient for high-precision spectrophotometric analysis. We find that the linear interpolation method applied to the A100_Z100_U10 grid offers the optimal balance between accuracy and computational efficiency.

B. EMULATING EMPIRICAL MAGNITUDE LIMITS OF AN IMAGING OBSERVATION

We validate `GalSyn`’s noise simulation framework against empirical data from the JADES survey. Specifically, we utilize a subregion of the JADES deep imaging, jw011800-deep field, with a total exposure time of approximately 87

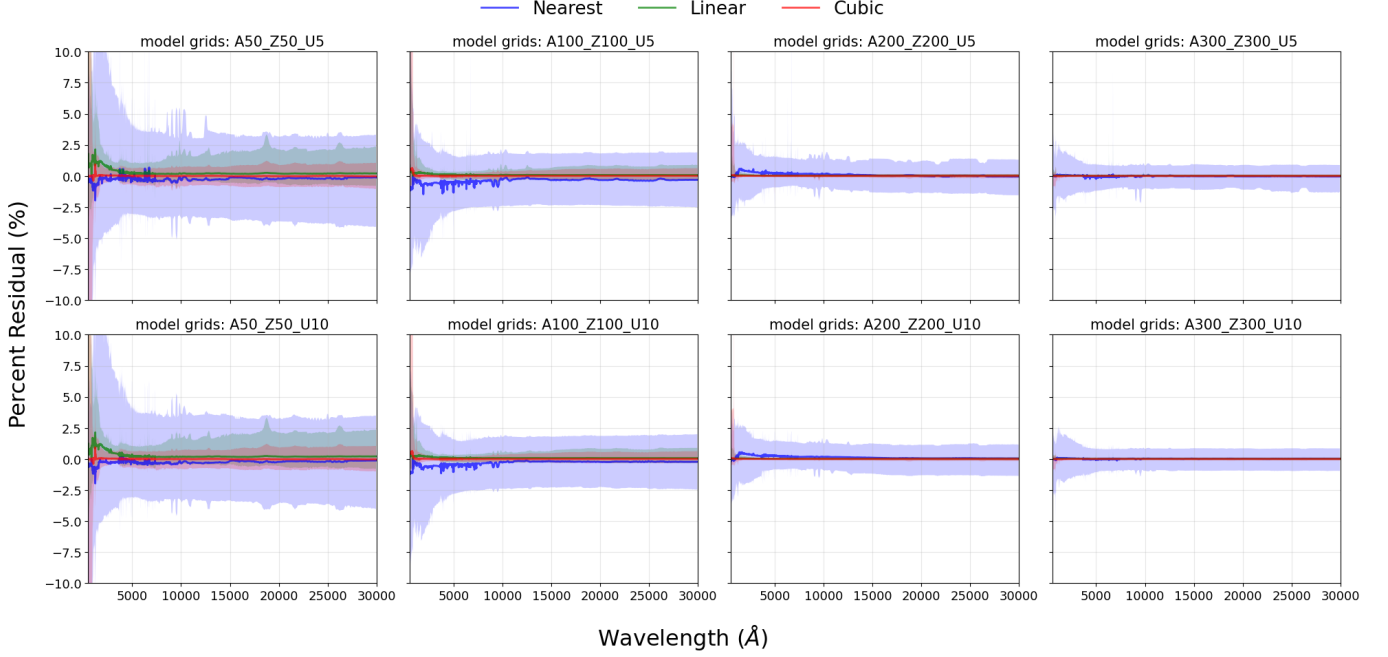


Figure 18. Percentage residuals between interpolated SSP+nebular spectra and ground-truth models across various grid configurations. The top row utilizes 5 ionization parameter bins ($U5$), while the bottom row utilizes 10 ($U10$). Different colors represent grid densities in age and metallicity (A and Z). The comparison demonstrates that while cubic interpolation (right column) is the most precise, linear interpolation (middle column) on a $100 \times 100 \times 10$ grid provides a high-fidelity recovery (residuals $\lesssim 1\%$) at a fraction of the computational cost.

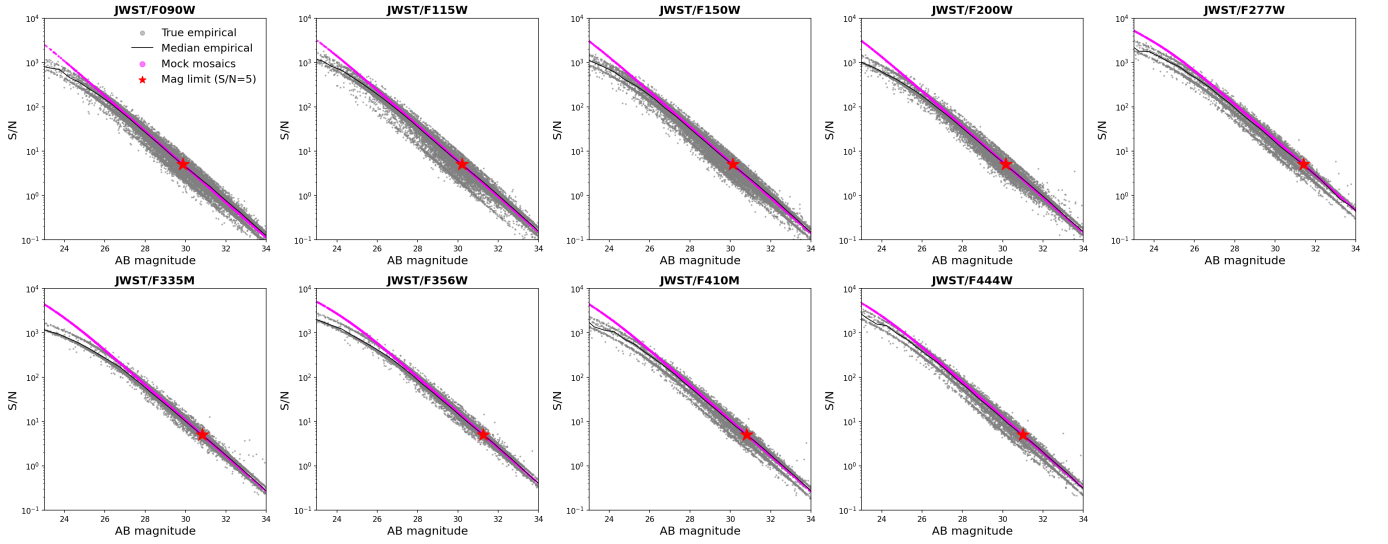


Figure 19. Comparison between the empirical and simulated S/N as a function of AB magnitude across nine NIRCcam filters. The grey data points represent the empirical relation derived from the JADES deep imaging observation of jw011800-deep field (87-hour exposure). The black line denotes the median relation. The magenta data points represent the S/N relation recovered by *GalSyn*. The red star symbols indicate the empirical $5 - \sigma$ limiting magnitude. *GalSyn* shows high fidelity in emulating the 5σ limiting magnitudes across all bands, with a slight overestimation of S/N for the brightest sources.

hours (B. D. Johnson et al. 2026). This deep baseline allows us to test the accuracy of our noise injection over a wide dynamic range of magnitudes across nine NIRCcam filters.

The noise simulation is designed to match the 5σ limiting magnitudes of the reference observation. Using the empirical limits (e.g., $m_{\text{lim}} \sim 29.88$ in F090W and $m_{\text{lim}} \sim 31.00$ in F444W), we inject noise into the TNG50-11-10 mosaic (see Figure 15) to recover the S/N vs. magnitude relation. As shown in Figure 19, `GalSyn` effectively recovers the median S/N-magnitude relation and the 5σ depth across all filters, confirming that the tool can reliably emulate the sensitivity of imaging surveys.

We note a slight discrepancy at the brightest end, where `GalSyn` tends to overestimate the S/N compared to the empirical JADES data. This offset likely stems from the simplified treatment of pixel-level saturation or non-linear noise components in the simulation, which become more prominent for high-flux sources. However, for the bulk of the galaxy population near the detection limits, which is the primary focus for high-redshift studies, the agreement is excellent, demonstrating the robustness of the noise simulation.

C. ESTIMATING MAGNITUDE LIMITS OF NIRSPEC IFU WITH JWST ETC

To simulate realistic observational noise in synthetic JWST/NIRSpec IFU datacubes, we conducted systematic S/N simulations using the `Pandemia` engine (K. M. Pontoppidan et al. 2016), the official exposure time calculator for JWST. We modeled a “flat” input spectrum (i.e., constant in AB magnitude) across a grid of source magnitudes ranging from 18 to 28 and for effective exposure times of 10, 20, and 40 ks. This experiment was carried out for nine primary instrument configurations: the high-resolution gratings (G140H/F070LP, G140H/F100LP, G235H/F170LP, and G395H/F290LP), the medium-resolution gratings (G140M/F070LP, G140M/F100LP, G235M/F170LP, and G395M/F290LP), and the low-resolution Prism/CLEAR mode. By calculating the S/N per pixel on the native detector grid, our model accounts for critical wavelength-dependent factors including instrument throughput, thermal background, and detector noise.

The resulting 5σ sensitivity limits, illustrated in Figure 20, reveal the depth achievable across the NIRSpec wavelength range. For a 40 ks exposure, the medium-resolution gratings typically reach limits between 24 and 26 mag. In contrast, the low-resolution Prism mode, even with a shorter 20 ks exposure, achieves significantly greater depth—exceeding 27 mag, due to its lower spectral resolution, spreading the signal over fewer pixels.

These calculated limits are integrated into the `GalSyn` post-processing suite to ensure observational realism in our mock datasets. We interpolate the magnitude–S/N relationship at every wavelength point to derive a continuous, wavelength-dependent sensitivity curve. This information is then passed to the `GalSyn` noise simulation module (Section 3.3). By scaling the noise variance according to the interpolated `Pandemia` results, we produce synthetic IFU observations that are statistically consistent with the expected performance of JWST. An example of a post-processed result is shown in Figure 10.

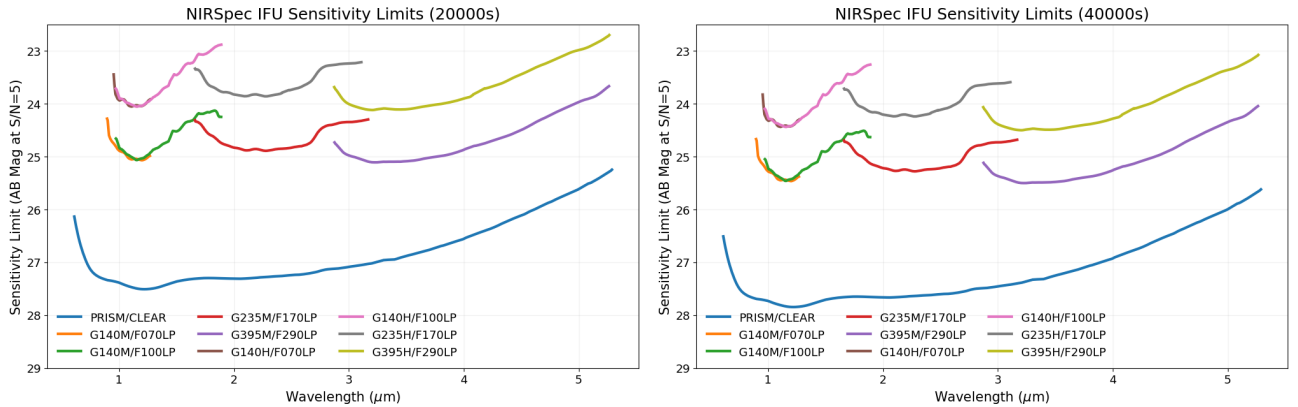


Figure 20. Estimated 5σ limiting magnitudes for JWST/NIRSpec IFU observations as a function of wavelength, derived from the `Pandemia` ETC engine (K. M. Pontoppidan et al. 2016). The left and right panels display the sensitivity limits for exposure times of 20 ks and 40 ks, respectively. The colored lines indicate the performance of the nine primary instrument configurations: the high-resolution gratings (G140H/F070LP, G140H/F100LP, G235H/F170LP, and G395H/F290LP), the medium-resolution gratings (G140M/F070LP, G140M/F100LP, G235M/F170LP, and G395M/F290LP), and the low-resolution Prism/CLEAR mode.

REFERENCES

- Abdurro'uf, Lin, Y.-T., Wu, P.-F., & Akiyama, M. 2021, *ApJS*, 254, 15, doi: [10.3847/1538-4365/abebe2](https://doi.org/10.3847/1538-4365/abebe2)
- Abdurro'uf, Lin, Y.-T., Wu, P.-F., & Akiyama, M. 2022, piXedfit: Analyze spatially resolved SEDs of galaxies,, Astrophysics Source Code Library, record ascl:2207.033
- Astropy Collaboration, Robitaille, T. P., Tollerud, E. J., et al. 2013, *A&A*, 558, A33, doi: [10.1051/0004-6361/201322068](https://doi.org/10.1051/0004-6361/201322068)
- Astropy Collaboration, Price-Whelan, A. M., Sipőcz, B. M., et al. 2018, *AJ*, 156, 123, doi: [10.3847/1538-3881/aabc4f](https://doi.org/10.3847/1538-3881/aabc4f)
- Baker, W. M., Valentino, F., Lagos, C. d. P., et al. 2025, *A&A*, 702, A270, doi: [10.1051/0004-6361/202555829](https://doi.org/10.1051/0004-6361/202555829)
- Battisti, A. J., Cunha, E. d., Shivaee, I., & Calzetti, D. 2020, *ApJ*, 888, 108, doi: [10.3847/1538-4357/ab5fdd](https://doi.org/10.3847/1538-4357/ab5fdd)
- Bressan, A., Marigo, P., Girardi, L., et al. 2012, *MNRAS*, 427, 127, doi: [10.1111/j.1365-2966.2012.21948.x](https://doi.org/10.1111/j.1365-2966.2012.21948.x)
- Bruzual, G., & Charlot, S. 2003, *MNRAS*, 344, 1000, doi: [10.1046/j.1365-8711.2003.06897.x](https://doi.org/10.1046/j.1365-8711.2003.06897.x)
- Calzetti, D., Armus, L., Bohlin, R. C., et al. 2000, *ApJ*, 533, 682, doi: [10.1086/308692](https://doi.org/10.1086/308692)
- Calzetti, D., Kinney, A. L., & Storchi-Bergmann, T. 1994, *ApJ*, 429, 582, doi: [10.1086/174346](https://doi.org/10.1086/174346)
- Camps, P., & Baes, M. 2015, *Astronomy and Computing*, 9, 20, doi: [10.1016/j.ascom.2014.10.004](https://doi.org/10.1016/j.ascom.2014.10.004)
- Camps, P., & Baes, M. 2020, *Astronomy and Computing*, 31, 100381, doi: [10.1016/j.ascom.2020.100381](https://doi.org/10.1016/j.ascom.2020.100381)
- Cardelli, J. A., Clayton, G. C., & Mathis, J. S. 1989, *ApJ*, 345, 245, doi: [10.1086/167900](https://doi.org/10.1086/167900)
- Carnall, A. C., McLure, R. J., Dunlop, J. S., & Davé, R. 2018, *MNRAS*, 480, 4379, doi: [10.1093/mnras/sty2169](https://doi.org/10.1093/mnras/sty2169)
- Carnall, A. C., McLure, R. J., Dunlop, J. S., et al. 2023, *Nature*, 619, 716, doi: [10.1038/s41586-023-06158-6](https://doi.org/10.1038/s41586-023-06158-6)
- Chabrier, G. 2003, *PASP*, 115, 763, doi: [10.1086/376392](https://doi.org/10.1086/376392)
- Chevallard, J., Charlot, S., Wandelt, B., & Wild, V. 2013, *MNRAS*, 432, 2061, doi: [10.1093/mnras/stt523](https://doi.org/10.1093/mnras/stt523)
- Choi, J., Dotter, A., Conroy, C., et al. 2016, *ApJ*, 823, 102, doi: [10.3847/0004-637X/823/2/102](https://doi.org/10.3847/0004-637X/823/2/102)
- Clayton, G. C., & Martin, P. G. 1985, *ApJ*, 288, 558, doi: [10.1086/162821](https://doi.org/10.1086/162821)
- Conroy, C., & Gunn, J. E. 2010, *ApJ*, 712, 833, doi: [10.1088/0004-637X/712/2/833](https://doi.org/10.1088/0004-637X/712/2/833)
- Conroy, C., Gunn, J. E., & White, M. 2009, *ApJ*, 699, 486, doi: [10.1088/0004-637X/699/1/486](https://doi.org/10.1088/0004-637X/699/1/486)
- da Cunha, E., Charlot, S., & Elbaz, D. 2008, *MNRAS*, 388, 1595, doi: [10.1111/j.1365-2966.2008.13535.x](https://doi.org/10.1111/j.1365-2966.2008.13535.x)
- Davé, R. 2008, *MNRAS*, 385, 147, doi: [10.1111/j.1365-2966.2008.12866.x](https://doi.org/10.1111/j.1365-2966.2008.12866.x)
- Draine, B. T. 2003, *ARA&A*, 41, 241, doi: [10.1146/annurev.astro.41.011802.094840](https://doi.org/10.1146/annurev.astro.41.011802.094840)
- Edmunds, M. G. 2001, *MNRAS*, 328, 223, doi: [10.1046/j.1365-8711.2001.04859.x](https://doi.org/10.1046/j.1365-8711.2001.04859.x)
- Eisenstein, D. J., Willott, C., Alberts, S., et al. 2026, *ApJS*, 283, 6, doi: [10.3847/1538-4365/ae3163](https://doi.org/10.3847/1538-4365/ae3163)
- Eisert, L., Pillepich, A., Nelson, D., et al. 2023, *MNRAS*, 519, 2199, doi: [10.1093/mnras/stac3295](https://doi.org/10.1093/mnras/stac3295)
- Eldridge, J. J., Stanway, E. R., Xiao, L., et al. 2017, *PASA*, 34, e058, doi: [10.1017/pasa.2017.51](https://doi.org/10.1017/pasa.2017.51)
- Euclid Collaboration, Mellier, Y., Abdurro'uf, et al. 2025, *A&A*, 697, A1, doi: [10.1051/0004-6361/202450810](https://doi.org/10.1051/0004-6361/202450810)
- Faucher, N., Blanton, M. R., & Macciò, A. V. 2023, *ApJ*, 957, 7, doi: [10.3847/1538-4357/acf9f0](https://doi.org/10.3847/1538-4357/acf9f0)
- Ferland, G. J., Korista, K. T., Verner, D. A., et al. 1998, *PASP*, 110, 761, doi: [10.1086/316190](https://doi.org/10.1086/316190)
- Ferland, G. J., Porter, R. L., van Hoof, P. A. M., et al. 2013, *RMxAA*, 49, 137. <https://arxiv.org/abs/1302.4485>
- Fitzpatrick, E. L. 1999, *PASP*, 111, 63, doi: [10.1086/316293](https://doi.org/10.1086/316293)
- Fortuni, F., Merlin, E., Fontana, A., et al. 2023, *A&A*, 677, A102, doi: [10.1051/0004-6361/202346725](https://doi.org/10.1051/0004-6361/202346725)
- Gardner, J. P., Mather, J. C., Abbott, R., et al. 2023, *PASP*, 135, 068001, doi: [10.1088/1538-3873/acd1b5](https://doi.org/10.1088/1538-3873/acd1b5)
- Girardi, L., Bressan, A., Bertelli, G., & Chiosi, C. 2000, *A&AS*, 141, 371, doi: [10.1051/aas:2000126](https://doi.org/10.1051/aas:2000126)
- Gordon, K. D., Clayton, G. C., Misselt, K. A., Landolt, A. U., & Wolff, M. J. 2003, *ApJ*, 594, 279, doi: [10.1086/376774](https://doi.org/10.1086/376774)
- Harvey, T., Lovell, C. C., Newman, S., et al. 2026, *MNRAS*, 547, stag282, doi: [10.1093/mnras/stag282](https://doi.org/10.1093/mnras/stag282)
- Haryana, N. S., Akiyama, M., Abdurro'uf, et al. 2025, *ApJ*, 994, 215, doi: [10.3847/1538-4357/ae03ad](https://doi.org/10.3847/1538-4357/ae03ad)
- Hollenbach, D., & McKee, C. F. 1979, *ApJS*, 41, 555, doi: [10.1086/190631](https://doi.org/10.1086/190631)
- Hollenbach, D., & Salpeter, E. E. 1971, *ApJ*, 163, 155, doi: [10.1086/150754](https://doi.org/10.1086/150754)
- Inoue, A. K., Shimizu, I., Iwata, I., & Tanaka, M. 2014, *MNRAS*, 442, 1805, doi: [10.1093/mnras/stu936](https://doi.org/10.1093/mnras/stu936)
- Ivezić, Ž., Kahn, S. M., Tyson, J. A., et al. 2019, *ApJ*, 873, 111, doi: [10.3847/1538-4357/ab042c](https://doi.org/10.3847/1538-4357/ab042c)
- Janulewicz, P., & Cui, W. 2025, *RAS Techniques and Instruments*, 4, rzaf027, doi: [10.1093/rasti/rzaf027](https://doi.org/10.1093/rasti/rzaf027)
- Johnson, B., Foreman-Mackey, D., Sick, J., et al. 2024, *dfm/python-fsps: v0.4.7, v0.4.7 Zenodo*, doi: [10.5281/zenodo.12447779](https://doi.org/10.5281/zenodo.12447779)
- Johnson, B. D., Robertson, B. E., Eisenstein, D. J., et al. 2026, *arXiv e-prints*, arXiv:2601.15954, doi: [10.48550/arXiv.2601.15954](https://doi.org/10.48550/arXiv.2601.15954)
- Jonsson, P. 2006, *MNRAS*, 372, 2, doi: [10.1111/j.1365-2966.2006.10884.x](https://doi.org/10.1111/j.1365-2966.2006.10884.x)

- Kennicutt, Jr., R. C. 1998, *ARA&A*, 36, 189, doi: [10.1146/annurev.astro.36.1.189](https://doi.org/10.1146/annurev.astro.36.1.189)
- Kriek, M., & Conroy, C. 2013, *ApJL*, 775, L16, doi: [10.1088/2041-8205/775/1/L16](https://doi.org/10.1088/2041-8205/775/1/L16)
- Kroupa, P. 2001, *MNRAS*, 322, 231, doi: [10.1046/j.1365-8711.2001.04022.x](https://doi.org/10.1046/j.1365-8711.2001.04022.x)
- Kroupa, P., & Boily, C. M. 2002, *MNRAS*, 336, 1188, doi: [10.1046/j.1365-8711.2002.05848.x](https://doi.org/10.1046/j.1365-8711.2002.05848.x)
- Krumholz, M. R., McKee, C. F., & Tumlinson, J. 2009, *ApJ*, 699, 850, doi: [10.1088/0004-637X/699/1/850](https://doi.org/10.1088/0004-637X/699/1/850)
- Lejeune, T., Cuisinier, F., & Buser, R. 1997, *A&AS*, 125, 229, doi: [10.1051/aas:1997373](https://doi.org/10.1051/aas:1997373)
- Lovell, C. C., Roper, W. J., Vijayan, A. P., et al. 2025, arXiv e-prints, arXiv:2508.03888, doi: [10.48550/arXiv.2508.03888](https://doi.org/10.48550/arXiv.2508.03888)
- Lupton, R., Blanton, M. R., Fekete, G., et al. 2004, *PASP*, 116, 133, doi: [10.1086/382245](https://doi.org/10.1086/382245)
- Madau, P. 1995, *ApJ*, 441, 18, doi: [10.1086/175332](https://doi.org/10.1086/175332)
- Marinacci, F., Vogelsberger, M., Pakmor, R., et al. 2018, *MNRAS*, 480, 5113, doi: [10.1093/mnras/sty2206](https://doi.org/10.1093/mnras/sty2206)
- Nagaraj, G., Forbes, J. C., Leja, J., Foreman-Mackey, D., & Hayward, C. C. 2022, *ApJ*, 932, 54, doi: [10.3847/1538-4357/ac6c80](https://doi.org/10.3847/1538-4357/ac6c80)
- Naiman, J. P., Pillepich, A., Springel, V., et al. 2018, *MNRAS*, 477, 1206, doi: [10.1093/mnras/sty618](https://doi.org/10.1093/mnras/sty618)
- Nandy, K., Morgan, D. H., Willis, A. J., Wilson, R., & Gondhalekar, P. M. 1981, *MNRAS*, 196, 955, doi: [10.1093/mnras/196.4.955](https://doi.org/10.1093/mnras/196.4.955)
- Narayanan, D., Turk, M. J., Robitaille, T., et al. 2021, *ApJS*, 252, 12, doi: [10.3847/1538-4365/abc487](https://doi.org/10.3847/1538-4365/abc487)
- Nelson, D., Pillepich, A., Springel, V., et al. 2018, *MNRAS*, 475, 624, doi: [10.1093/mnras/stx3040](https://doi.org/10.1093/mnras/stx3040)
- Nelson, D., Springel, V., Pillepich, A., et al. 2019a, *Computational Astrophysics and Cosmology*, 6, 2, doi: [10.1186/s40668-019-0028-x](https://doi.org/10.1186/s40668-019-0028-x)
- Nelson, D., Pillepich, A., Springel, V., et al. 2019b, *MNRAS*, 490, 3234, doi: [10.1093/mnras/stz2306](https://doi.org/10.1093/mnras/stz2306)
- Noll, S., Pierini, D., Cimatti, A., et al. 2009, *A&A*, 499, 69, doi: [10.1051/0004-6361/200811526](https://doi.org/10.1051/0004-6361/200811526)
- Perrin, M. D., Sivaramakrishnan, A., Lajoie, C.-P., et al. 2014, in *Society of Photo-Optical Instrumentation Engineers (SPIE) Conference Series*, Vol. 9143, *Space Telescopes and Instrumentation 2014: Optical, Infrared, and Millimeter Wave*, ed. J. M. Oschmann, Jr., M. Clampin, G. G. Fazio, & H. A. MacEwen, 91433X, doi: [10.1117/12.2056689](https://doi.org/10.1117/12.2056689)
- Pietrinferni, A., Cassisi, S., Salaris, M., & Castelli, F. 2004, *ApJ*, 612, 168, doi: [10.1086/422498](https://doi.org/10.1086/422498)
- Pillepich, A., Nelson, D., Hernquist, L., et al. 2018, *MNRAS*, 475, 648, doi: [10.1093/mnras/stx3112](https://doi.org/10.1093/mnras/stx3112)
- Pillepich, A., Nelson, D., Springel, V., et al. 2019, *MNRAS*, 490, 3196, doi: [10.1093/mnras/stz2338](https://doi.org/10.1093/mnras/stz2338)
- Pontoppidan, K. M., Pickering, T. E., Laidler, V. G., et al. 2016, in *Society of Photo-Optical Instrumentation Engineers (SPIE) Conference Series*, Vol. 9910, *Observatory Operations: Strategies, Processes, and Systems VI*, ed. A. B. Peck, R. L. Seaman, & C. R. Benn, 991016, doi: [10.1117/12.2231768](https://doi.org/10.1117/12.2231768)
- Prevot, M. L., Lequeux, J., Maurice, E., Prevot, L., & Rocca-Volmerange, B. 1984, *A&A*, 132, 389
- Reddy, N. A., Topping, M. W., Sanders, R. L., Shapley, A. E., & Brammer, G. 2023a, *ApJ*, 952, 167, doi: [10.3847/1538-4357/acd754](https://doi.org/10.3847/1538-4357/acd754)
- Reddy, N. A., Sanders, R. L., Shapley, A. E., et al. 2023b, *ApJ*, 951, 56, doi: [10.3847/1538-4357/acd0b1](https://doi.org/10.3847/1538-4357/acd0b1)
- Rigby, J., Perrin, M., McElwain, M., et al. 2023, *PASP*, 135, 048001, doi: [10.1088/1538-3873/acb293](https://doi.org/10.1088/1538-3873/acb293)
- Robitaille, T. P. 2011, *A&A*, 536, A79, doi: [10.1051/0004-6361/201117150](https://doi.org/10.1051/0004-6361/201117150)
- Rodriguez-Gomez, V., Genel, S., Vogelsberger, M., et al. 2015, *MNRAS*, 449, 49, doi: [10.1093/mnras/stv264](https://doi.org/10.1093/mnras/stv264)
- Rodriguez-Gomez, V., Sales, L. V., Genel, S., et al. 2017, *MNRAS*, 467, 3083, doi: [10.1093/mnras/stx305](https://doi.org/10.1093/mnras/stx305)
- Roper, W. J., Lovell, C. C., Vijayan, A., et al. 2026, *Journal of Open Source Software*, 11, 9436, doi: [10.21105/joss.09436](https://doi.org/10.21105/joss.09436)
- Rowe, B. T. P., Jarvis, M., Mandelbaum, R., et al. 2015, *Astronomy and Computing*, 10, 121, doi: [10.1016/j.ascom.2015.02.002](https://doi.org/10.1016/j.ascom.2015.02.002)
- Salim, S., Boquien, M., & Lee, J. C. 2018, *ApJ*, 859, 11, doi: [10.3847/1538-4357/aabf3c](https://doi.org/10.3847/1538-4357/aabf3c)
- Salim, S., & Narayanan, D. 2020, *ARA&A*, 58, 529, doi: [10.1146/annurev-astro-032620-021933](https://doi.org/10.1146/annurev-astro-032620-021933)
- Salmon, B., Papovich, C., Long, J., et al. 2016, *ApJ*, 827, 20, doi: [10.3847/0004-637X/827/1/20](https://doi.org/10.3847/0004-637X/827/1/20)
- Salpeter, E. E. 1955, *ApJ*, 121, 161, doi: [10.1086/145971](https://doi.org/10.1086/145971)
- Sánchez-Blázquez, P., Peletier, R. F., Jiménez-Vicente, J., et al. 2006, *MNRAS*, 371, 703, doi: [10.1111/j.1365-2966.2006.10699.x](https://doi.org/10.1111/j.1365-2966.2006.10699.x)
- Schaller, G., Schaerer, D., Meynet, G., & Maeder, A. 1992, *A&AS*, 96, 269
- Schaye, J., Crain, R. A., Bower, R. G., et al. 2015, *MNRAS*, 446, 521, doi: [10.1093/mnras/stu2058](https://doi.org/10.1093/mnras/stu2058)
- Schaye, J., Chaikin, E., Schaller, M., et al. 2025, arXiv e-prints, arXiv:2508.21126, doi: [10.48550/arXiv.2508.21126](https://doi.org/10.48550/arXiv.2508.21126)
- Smail, I., Dudzevičiūtė, U., Stach, S. M., et al. 2021, *MNRAS*, 502, 3426, doi: [10.1093/mnras/stab283](https://doi.org/10.1093/mnras/stab283)
- Snyder, G. F., Peña, T., Yung, L. Y. A., et al. 2023, *MNRAS*, 518, 6318, doi: [10.1093/mnras/stac3397](https://doi.org/10.1093/mnras/stac3397)

- Somerville, R. S., Gilmore, R. C., Primack, J. R., & Domínguez, A. 2012, MNRAS, 423, 1992, doi: [10.1111/j.1365-2966.2012.20490.x](https://doi.org/10.1111/j.1365-2966.2012.20490.x)
- Sommovigo, L., Cochrane, R. K., Somerville, R. S., et al. 2025, ApJ, 990, 114, doi: [10.3847/1538-4357/addec1](https://doi.org/10.3847/1538-4357/addec1)
- Springel, V., Pakmor, R., Pillepich, A., et al. 2018, MNRAS, 475, 676, doi: [10.1093/mnras/stx3304](https://doi.org/10.1093/mnras/stx3304)
- van Dokkum, P. G. 2008, ApJ, 674, 29, doi: [10.1086/525014](https://doi.org/10.1086/525014)
- Vogelsberger, M., Nelson, D., Pillepich, A., et al. 2020, MNRAS, 492, 5167, doi: [10.1093/mnras/staa137](https://doi.org/10.1093/mnras/staa137)
- Williams, R. J., Quadri, R. F., Franx, M., van Dokkum, P., & Labbé, I. 2009, ApJ, 691, 1879, doi: [10.1088/0004-637X/691/2/1879](https://doi.org/10.1088/0004-637X/691/2/1879)
- Yung, L. Y. A., Somerville, R. S., Finkelstein, S. L., Popping, G., & Davé, R. 2019, MNRAS, 483, 2983, doi: [10.1093/mnras/sty3241](https://doi.org/10.1093/mnras/sty3241)